Title

Water absorption and shrinkage behaviour of early-age cement in wellbore annulus

1 Introduction

Cementing operations in oil and gas wells are often performed under an assumption that cement shrinkage is negligible in terms of well-formation interaction. However, if the hardening cement slurry is surrounded by low permeability formation, large bulk volume shrinkage can occur because the cement cannot absorb sufficient water from the formation to compensate for its hydration process. Although there are several reported studies on cement shrinkage behaviour in the laboratory, the measured bulk shrinkage volumes may not be representative under the wellbore conditions. It is hypothesised in this study that a proper evaluation of cement shrinkage volume is crucial for assessing the wellbore and formation integrity prior to oil/gas production.

Various bulk shrinkage values of typical oil well cements are reported in the literature. As shown by a summary given in Table 1, a wide range of bulk shrinkage volume between 0.1% and 7.15% of the original volume is reported. It is generally known that cement bulk shrinkage behaviour is affected by many different factors, such as temperature and pressure and employed test methods (Reddy et al. 2009). High curing temperature changes the cement hydration chemistry in such a way that hydration temperature has two peaks, resulting in the S-shaped shrinkage curve (Lyomov et al. 1997). For Class G cement, Goboncan & Dillenbeck 2003 showed in their laboratory-scale high-pressure and high-temperature cement shrinkage tests that the bulk shrinkage volume was 0.1% at 100 h after cement mixing under the curing condition of 20 MPa and 150^{o}C. The bulk shrinkage volume of Class G cement decreases with decreasing water-to-cement ratio as well as with increasing amount of calcium carbonate and polyvinyl alcohol (PVA) (Justnes et al. 1995). Also, shrinkage volume reduces by decreasing cement contents (Backe et al. 1999) and by adding bonding agents (Parcevaux & Sault 1984). Shrinkage test results on Class H cement also show that the bulk shrinkage volume decreases with decreasing amount of available water for cement hydration which is achieved by increasing the temperature and pressure as well as using water-consuming additives such as sodium chloride, silica flour, bentonite, or sodium silicate (Chenevert & Shrestha 1991). For instance, the bulk shrinkage volume of Class H cement cured under 8.3 MPa and 38^{o}C typically reaches its asymptotic value of 3.8% in 70 h (Chenevert & Shrestha 1987).

Table 1 Bulk shrinkage volume values of oil/gas well cements measured in the laboratory.

	Cement type	Water-to-cement ratio	Additives	Temperature (°C)	Pressure (MPa)	Drainage	Test duration (h)	Shrinkage volume (%)
Backe et al. (1999)	Class G	0.44	Retarder	90	0.0025	Open	20	3.92
Chenevert et al. (1991)	Class H	N/A	Retarder	37.8, 65.6, 93.3	8.27, 24.1, 35.9	Closed	70	4.3, 3.8, 3.4
Goboncan et al. (2003)	Class G	N/A	Fluid loss control, dispersant	149	19.3	Open	110	0.1
Justnes et al. (1995)	Class G	0.3, 0.4, 0.5	None	20	Ambient pressure	Closed	48	2.2, 1.5, 1.1
Lyomov et al. (1997)	N/A	N/A	Retarder	25, 60,	0.6~1.6	Open	24	3.7, 3.5
Parcevaux & Sault (1984)	Class G	0.44	Dispersant, retarder	20	0.5, 4.0, 10.0	Closed	48	7.15, 6.30, 4.30
Reddy et al. (2009)	N/A	N/A	Defoamer	26.7	0, 6.89, 13.8, 20.7	Closed	70	1.3, 3.1, 3.6, 3.8

Despite the uncertainty in the magnitude of cement shrinkage volume in actual wellbore annuli, the effect of cement shrinkage volume on wellbore integrity has been examined in the past by numerical simulations of the problem. For example, Ravi et al. (2002) showed that, the smaller the cement shrinkage volume is, the less the risk of cement failure such as fracture, plastic deformation and debonding becomes. Oyarhossein & Dusseault (2015) reported that the combination of stiff formation and cement shrinkage volume would increase the risk of loss of zonal isolation because stiff formation could not follow cement shrinkage to prevent debonding at the interface. However, they stated that cement data under the downhole conditions would be necessary to improve their numerical model. Gray et al. (2007) built a 3D model that incorporated the non-linear mechanical behaviour of cement and formation and showed that cement shrinkage could lead to debonding between casing-cement interface because of plastic straining of the formation reaching their maximum values in the direction of the minimum horizontal stress. In the abovementioned studies, uniform shrinkage volume is specified over the entire cement elements and it is noted that the values used for cement shrinkage volume are different (i.e., 0% and 4% (Ravi et al. 2002), 0.5% (Oyarhossein & Dusseault 2015), and 5% (Gray et al. 2007)). Saint-Marc et al. (2008) incorporated a volumetric strain term arising from cement shrinkage, which was correlated with change in the degree of cement hydration, in the isotropic elastic constitutive equation to model cement shrinkage behaviour. However, pore fluid flow was not coupled with the constitutive equation.

Cement shrinkage behaviour is characterized by the development of capillary suction pressure in the pores of cement material as water is consumed by hydrating cement particles. Hua et al. (1995) show in their tests on early-age cement paste that cement shrinkage after the initial set (i.e. the thickening time) can be estimated by calculating the capillary suction development during the cement hardening process and by using it as confining pressure on an elastic porous body with time-varying stiffness. Lura et al. (2003) incorporate the degree of water saturation as a coefficient to calculate the confining stress caused by the capillary suction pressure and incorporate the stiffness of the cement particles in addition to the bulk stiffness of the cement skeleton, to accurately predict the linear shrinkage volume of early-age cement paste. By conducting a thermo-hydro-mechanical coupled simulation on early-age cement shrinkage, Zhen & Xiong (2013) find that the contribution from thermal strain is pronounced during the first 5h of the shrinkage since the initial set but becomes negligible after 24h. The capillary suction pressure concept for estimating cement shrinkage volume is also found effective for post early-age cement (Coussy et al. 2004). Rougelot et al. (2009) show that the capillary suction pressure concept is valid for hardened cement and argue the influence of cement particle stiffness and cement bulk stiffness in estimating cement shrinkage volume.

Considering the abovementioned findings on the physics of cement shrinkage, it is more realistic to carry out a hydro-mechanical coupled simulation on a porous cement material by utilising the capillary suction pressure concept rather than specifying uniform shrinkage over the entire cement. By doing so, the bulk shrinkage behaviour of early-age cement and the associated wellbore behaviour can be evaluated for more realistic scenarios. An earlier attempt of such simulation was made by Thiercelin et al. (1998) who introduced a fluid sink term in the hydro-mechnical coupled simulation as it can be directly related to the water consumption of a porous material during hydration. Bois et al. (2011) and Bois et al. (2012) also simulated the behaviour of annular cement as a porous material and modelled cement shrinkage volume by changing the pore pressure in their simulations. It is noted that capillary suction pressure (p_g-p_l) reduces to pore liquid pressure (p_l) when the cement pore space is fully saturated (p_g=0) and cavitation is unlikely to occur due to high liquid pressure (e.g. offshore cementing).

This study extends the work of Thiercelin et al. (1998) by conducting a coupled hydro-mechanical finite element analysis to simulate the water migration, absorption and volume shrinkage behaviour of early-age cement in a wellbore configuration. The primary objectives of this study are (i) to determine the threshold permeability value of the formation below which the cement cannot absorb adequate water from the formation to compensate for the water consumption by

the hydration reaction and (ii) to estimate a reasonable range of cement shrinkage volume in downhole conditions. The wellbore is modelled to be placed in the overburden of the Nankai Trough in Japan (Yamamoto et al. 2014), where the cement is surrounded by the low permeability clay formation on the outer boundary and by impermeable casing on the inner boundary. The mechanical and hydrological parameters of hardening cement paste are calibrated by utilizing laboratory test data on three different types of cement: Class G cement, rapid setting (RS) cement and optimized particle size distribution (OPSD) technology cement from Schlumberger.

2 Mechanism of cement shrinkage

The bulk shrinkage of cement can occur by three different mechanisms: (i) capillary depression effect, (ii) surface tension effect, and (iii) disjoining pressure effect (Hua et al. 1995). One or more of these mechanisms are dominant over the others depending on the relative humidity of the cement. For example, the capillary depression effect is the dominant mechanism at high relative humidity (i.e. over 80%) whereas the other two mechanisms are activated at lower relative humidity levels (i.e. below 45%) (Rougelot et al. 2009; Lura et al. 2003; Hua et al. 1995). The relative humidity of early-age cement paste is known not to decease below 75% even though it is left in contact with the air (Lura et al. 2003). Therefore, in the wellbore condition where the cement is surrounded by water-saturated formation, the primary mechanism of cement bulk shrinkage volume is the depression of capillary suction pressure (i.e. pore pressure). Such phenomena can be simulated by the coupled hydro-mechanical equations for porous materials; the hydraulic part of the equations is derived from the conservation of fluid mass in a porous media, whereas the mechanical part is derived from the force equilibrium.

The poromechanical approach to simulate the behaviours of cement paste has been found valid by Ulm et al. (2004). Unlike soils in which the bulk stiffness values of both soil grains and pore water are assumed to be very large relative to the stiffness of soil skeleton, the cement skeleton after hardening can be as stiff as the cement particles and pore water (Vu et al. 2012). Thus, the stiffness values of cement particles and pore water must be included in the constitutive equation. The modelling of cement bulk shrinkage is analogous to that of rocks, in which the stiffness of the solid phase in addition to that of the bulk porous material must be considered in the constitutive equations (Biot 1962; Nur & Byerlee 1971; Garg & Nur 1973). In addition, since the stiffness of early-age cement evolves with time, the volumetric shrinkage strain needs to be calculated in increments using Equation 1:

$$d\varepsilon_v = \int \frac{(d\sigma_m - \alpha du)}{K} \tag{1}$$

where $d\varepsilon_v$ is the volumetric strain increment, $d\sigma_m$ is the mean stress increment, du is the pore pressure increment, K is the time (or hardening) dependent bulk modulus of cement skeleton and α is the Biot-Willis coefficient (Biot & Willis 1957). The cement placed in wellbore annulus is often surrounded by a water-saturated formation under high hydrostatic pressure, which prevents the cavitation of the pore water and keeps the cement fully saturated. Hence, the effect of degree of saturation on the stress increment is not considered in this study.

The incremental form of constitutive equation for the cement skeleton is also employed in Hua et al. (1995) and Zhen & Xiong (2013) to calculate the volumetric shrinkage strain. Experimental observations (Maharidge et al. 2016; Teodoriu et al. 2012) indicate that the stiffness of early-age cement increases significantly with time. In this study, the incremental linear isotropic elasticity with time-varying stiffness is employed to model the observed cement shrinkage behaviour. This allows the simple linear isotropic elasticity to be employed to calculate irreversible strains due to the evolution of the skeleton stiffness of the cement. Plasticity models could also be used to simulate the volumetric shrinkage behaviour with the elastic stiffness maintained constant (Thiercelin et al. 1998). However, the determination of plasticity model parameters for early-age cement is very difficult.

The main model input is the sink term (i.e. volumetric strain of the pore fluid) in the fluid mass conservation equation. This term governs the loss of pore water due to the hydration reaction of cement particles, which leads to the depression of pore pressure and hence shrinkage volume. The stiffness and permeability of the cement are assumed to be time-dependent. Their time dependency changes are evaluated by laboratory test data available in literature, which is discussed in the next section.

3 Modelling of laboratory tests on cement shrinkage

3.1 Model dimensions and material parameters

The poromechanical framework for modelling the shrinkage behaviour of early-age cement is validated against laboratory test data on three different cement types: Class G cement, rapid setting (RS) cement (Appleby & Wilson 1996) and OPSD cement (Thomas et al. 2015). The material composition of RS cement is identical to that of Class G except for the extra amount of gypsum replacing cement particles to accelerate the initial set (i.e. the thickening time). OPSD cement is a light weight cement containing hollow fly ash particles and is designed for the cementing of shallow unconsolidated formation. OPSD cement was employed for the cementing operation of wellbores in the Nankai Trough in Japan (Taoutaou et al. 2014; Qiu et al. 2015).

In this study, the experimental work of Appleby & Wilson (1996) and Thomas et al. (2015) are simulated. The test setups of the cement specimens simulated in this study are shown in Figure 1. Two types of tests are usually conducted to examine the shrinkage behaviour of early-age cement; (i) drainage valve open (drained) and (ii) drainage value closed (undrained). In the former test, water is provided from the bottom port to the specimen and the amount of water absorbed into the specimen is recorded. In the latter test, the bulk shrinkage volume of the specimens is recorded instead of the absorbed water volume. The pore pressure data were available only for the Class G and RS cement tests. The applied pressure for the Class G and RS cement tests was 2 MPa whereas that for the OPSD cement test was 10 MPa. The temperature was maintained at approximately 20ºC for the Class G and RS tests and 12ºC for the OPSD cement test.

The ABAQUS finite element (FE) analysis software package is employed to carry out the coupled transient fluid flow and stress analysis. Since the geometry of the cement specimen is cylindrical (i.e. ϕ45 mm$\times$150 mm for the Class G and RS cement tests and ϕ45 mm$\times$25 mm for the OPSD cement test), axi-symmetric analysis is conducted. The finite element models (FEM) are shown in Figure 2. The models are discretized into 2250 axi-symmetric eight-node biquadratic displacement, bilinear pore pressure elements. For the boundary conditions, the constant pore pressure equal to the initial pore pressure is specified at the bottom boundary nodes to simulate the open valve tests, whereas no fluid flux is specified to simulate the closed valve tests.

The bulk modulus of cement particles and water are 21 GPa, and 2.2 GPa, respectively. As described earlier, the calibrated model parameters are the time-dependent values of sink rate (i.e. the rate of volumetric strain change of the pore water), permeability and Young's modulus. A constant Poisson's ratio of 0.20 is adopted. Although it may be argued that the cement at its fluid-like stage is in close to incompressible condition, it is assumed that the shear resistance develops rapidly prior to the initial set. The porosity is set to be constant at 0.25. This assumption is employed because the porosity parameter in the simulation does not affect the amount of water consumption by the cement; the sink rate determines it. Porosity does not affect the mechanical behavour, either, because Young's modulus and Poisson's ratio are specified independently of porosity in this study. These input parameters for the FEM for laboratory cement shirnkage tests are summarized in Table 2.

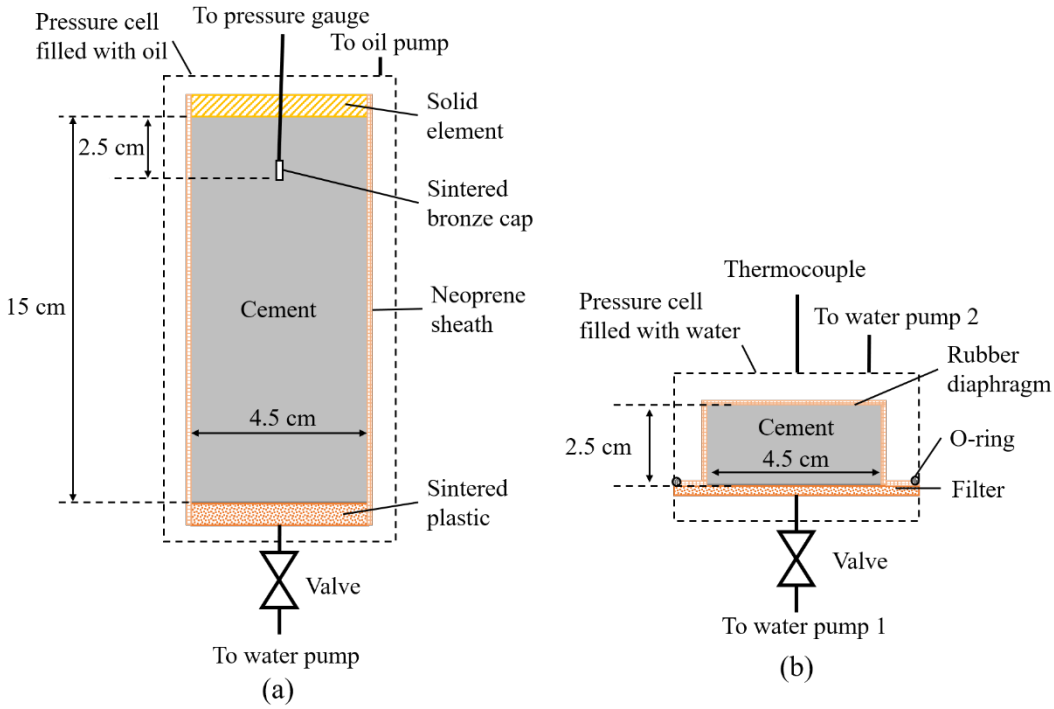

Figure 1 Test setups of the laboratory tests on cement shrinkage: (a) Class G cement and RS cement [after Appleby & Wilson (1996)]; (b) OPSD cement [after Thomas et al. (2015)].

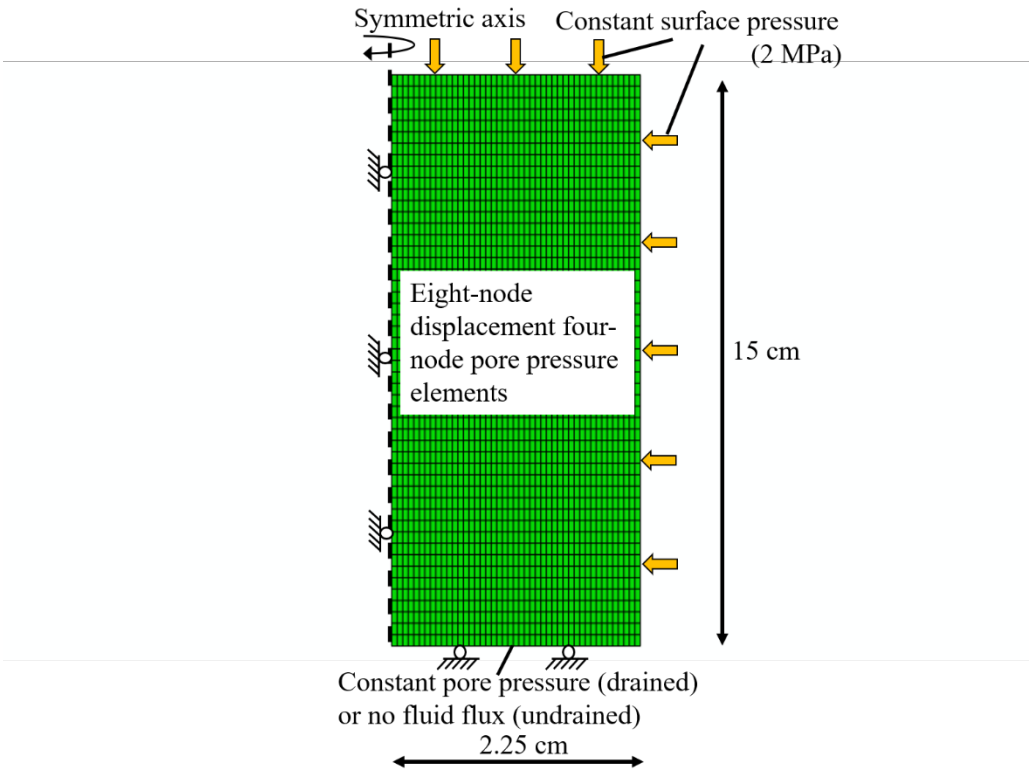

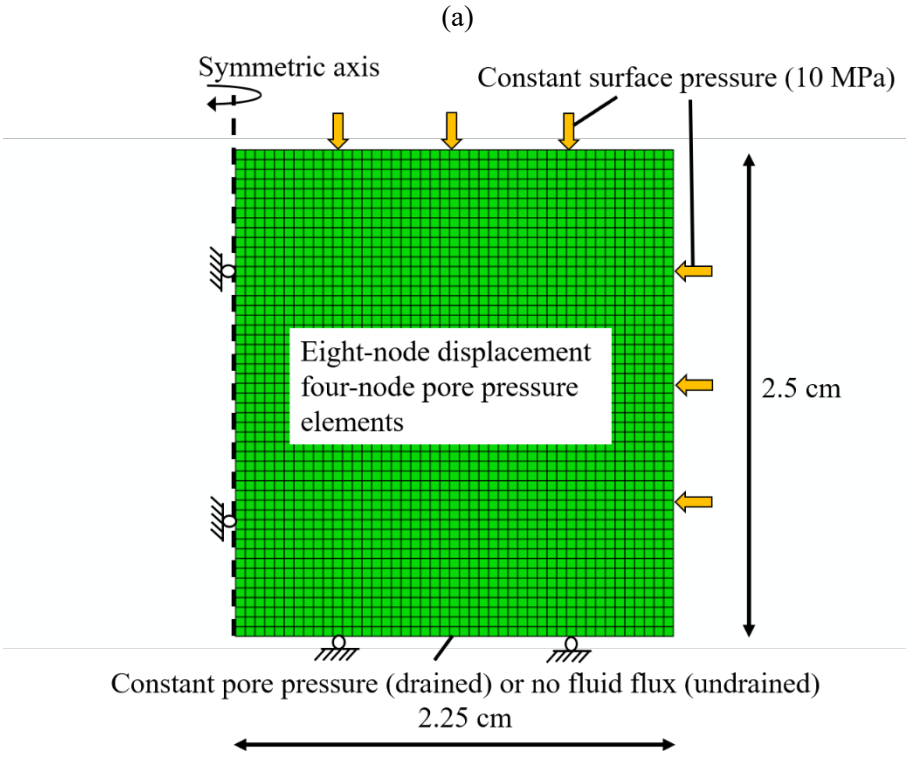

Figure 2 Finite element models (FEM) for the laboratory tests on cement shrinkage: (a) Class G cement and RS cement tests (enlarged three times in the horizontal direction); (b) OPSD cement test (to scale).

Table 2 Hydromechanical input parameters for the FEM for the laboratory tests on cement shrinkage.

Bulk modulus of cement particles	21 GPa
Bulk modulus of water	2.2 GPa
Poisson's ratio	0.2
Porosity	0.25
Sink rate	Figure 3a
Permeability	Figure 3b
Young's modulus	Figure 3c

3.2 Calibrated time-dependent sink rate, permeability and stiffness

The calibrated time-dependent sink rate, permeability, and Young's modulus are shown in Figure 3a, 3b and 3c, respectively. An exponential function is employed to model the time variations of these parameters. The origin of the time corresponds to the time of the initial set. The sink rate is assumed to monotonically decrease from its maximum at t = 0 to an asymptote. A large initial

sink rate is assigned for RS cement reflecting the fast reaction of gypsum. The sink rate of RS cement intersects with that of Class G cement at t = 18 h, after which the sink rates of Class G and RS cements are set to be identical. OPSD cement has an initial sink rate smaller than that of Class G and RS cements because OPSD cement has less amount of cement clinkers. The asymptotic sink rate of OPSD cement is larger than those of the other two cements because of the slow reaction of fly ash particles.

The initial permeability is set to 1 mD for Class G cement and OPSD cement, whereas it is set to 0.1 mD for RS cement to reflect the early ettringite formation. The final permeability is 1 μD for Class G and RS cements and 4 μD for OPSD cement.

Due to limited data on the initial Young's modulus measurement of early-age cement, the initial values are set to be roughly one hundredth of the final values for all cements. The Young's modulus values of Class G and RS cements change from the initial value of 50 MPa to the final value of 16 GPa, whereas the Young's modulus value of OPSD cement changes from 20 MPa to 3.81 GPa. The development of permeability and Young's modulus for RS cement is assumed to be delayed until t = 15 h due to the delayed hydration reaction of cement clinkers caused by the early formation of ettringite (Appleby & Wilson 1996).

The calibration of these model parameters was carried out in the following manner based on the findings from the parametric study of the effect of each parameter on cement shrinkage behaviour. First, the time-dependent sink rate was calibrated to match the computed absorbed water volume to the experimental result since the change in the permeability and Young's modulus had little effect on the computed absorbed water volume. Next, time-dependent Young's modulus was calibrated to match the computed bulk shrinkage with the experimental result due to the insensitivity of the permeability on the computation of bulk shrinkage volume. Finally, the time-dependent permeability was calibrated to match the computed pore pressure to the experiment data. Since pore pressure data were not available for the OPSD cement test, a reasonable initial value and the rate of permeability decrease were assumed for OPSD cement. The ultimate permeability value of OPSD cement (0.04 mD) was taken from Thomas et al. (2015).

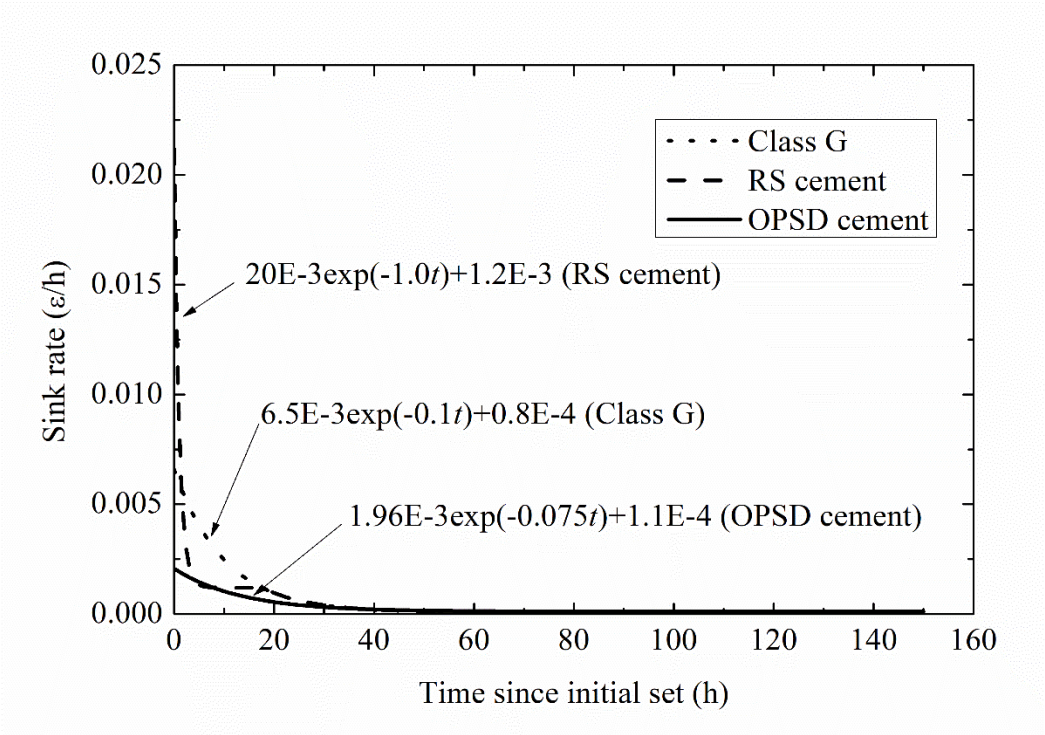
0.025
0.020
0.015
0.010
0.005
0.000
Sink rate (ε/h)
0
20
40
60
80
100
120
140
160
Time since initial set (h)
Class G
RS cement
OPSD cement
20E-3exp(-1.0t)+1.2E-3 (RS cement)
6.5E-3exp(-0.1t)+0.8E-4 (Class G)
1.96E-3exp(-0.075t)+1.1E-4 (OPSD cement)

(a)

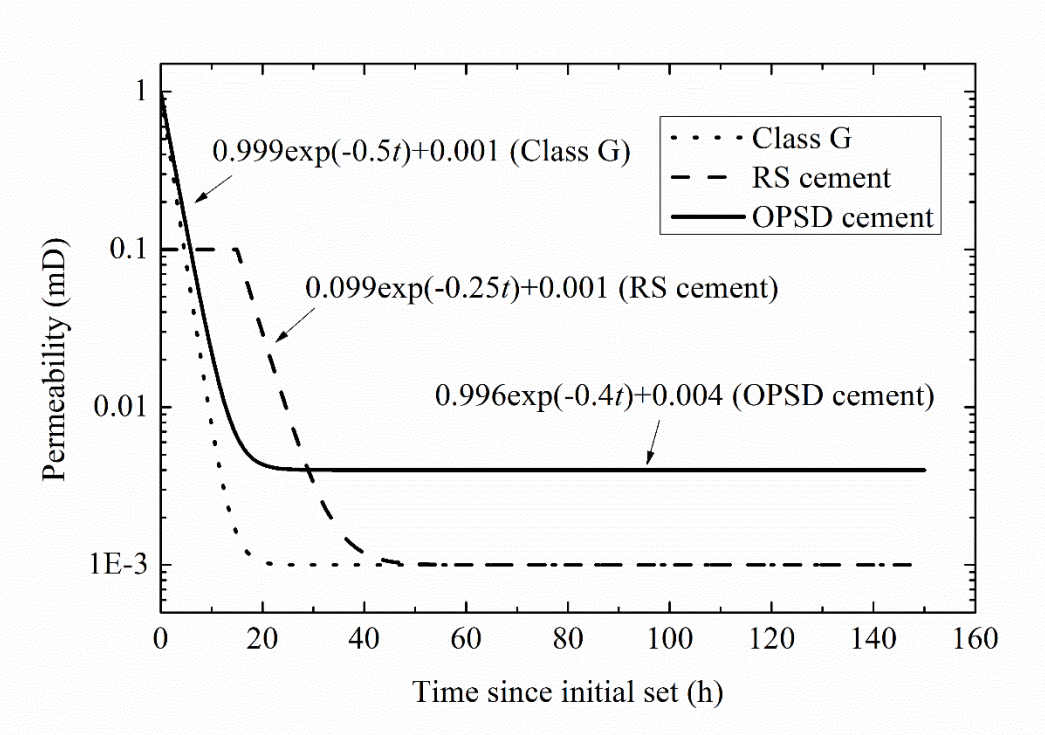
1
0.1
0.01
1E-3
Permeability (mD)
0
20
40
60
80
100
120
140
160
Time since initial set (h)
Class G
RS cement
OPSD cement
0.999exp(-0.5t)+0.001 (Class G)
0.099exp(-0.25t)+0.001 (RS cement)
0.996exp(-0.4t)+0.004 (OPSD cement)

(b)

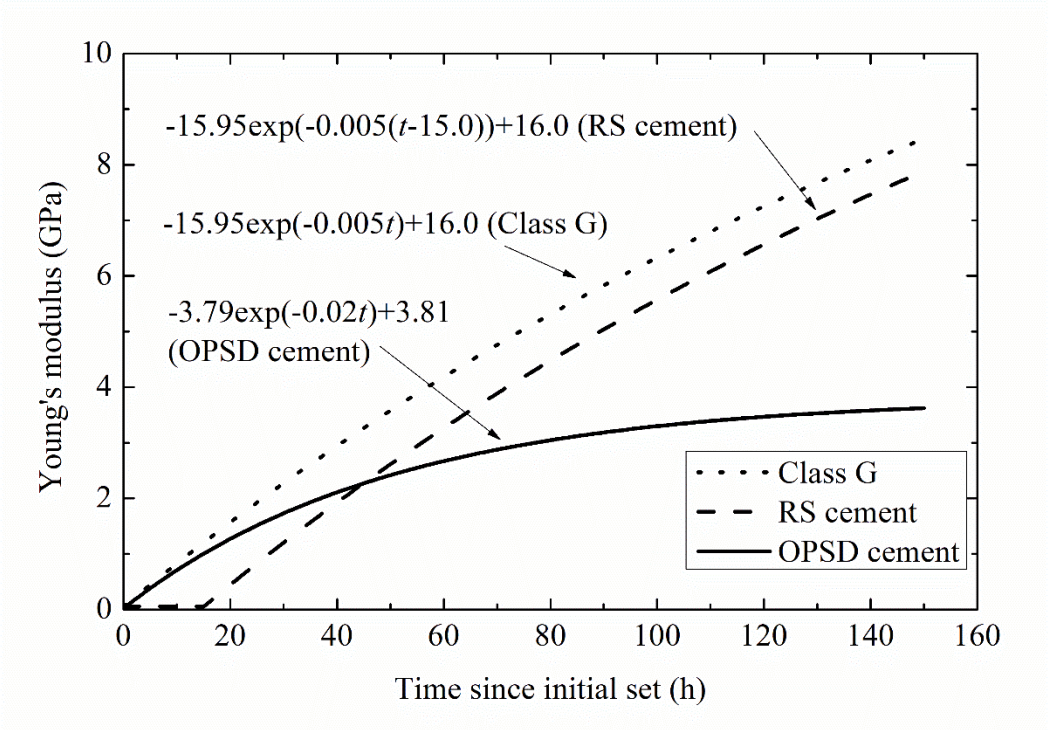

(c)

Figure 3 Calibrated time-dependent model parameters of cements: (a) sink rate; (b) permeability; (c) Young's modulus.

3.3 Results

The model calibration results for the three cement tests are shown in Figure 4. The time axis indicates the time after the initial set of the cement. The data from the period from the mixing of the cement to the initial set, t_{set}, (i.e. the thickening time) are removed. The shrinkage before the initial set is compensated for by the drop of the cement slurry column in the annulus (Thiercelin et al. 1998; Backe et al. 1999). Hence, the shrinkage after the initial set is relevant in this study.

As shown in Figure 4, there is good agreement between the experiments and simulations. The time-dependent behaviours of the absorbed water and shrinkage volumes are captured adequately for all cement types. The time scale of the Class G cement data is limited to a short period of several hours after the initial cement set. Hence it is not possible to calibrate beyond this time. As a result, the calculated bulk shrinkage volume of Class G cement seems to slightly overestimate its typical shrinkage volume (Reddy et al. 2009) (see Figure 4a). The agreement in the pore pressure curves (Figure 4c) is satisfactory until the simulation calculates pore water pressure much smaller than the experiment near the end of the time scale. This is probably due to the formation

of air bubbles in the cement pores in the experiment which decreases pore pressure levels. The produced air is initially dissolved in the pore water under high pore pressure.

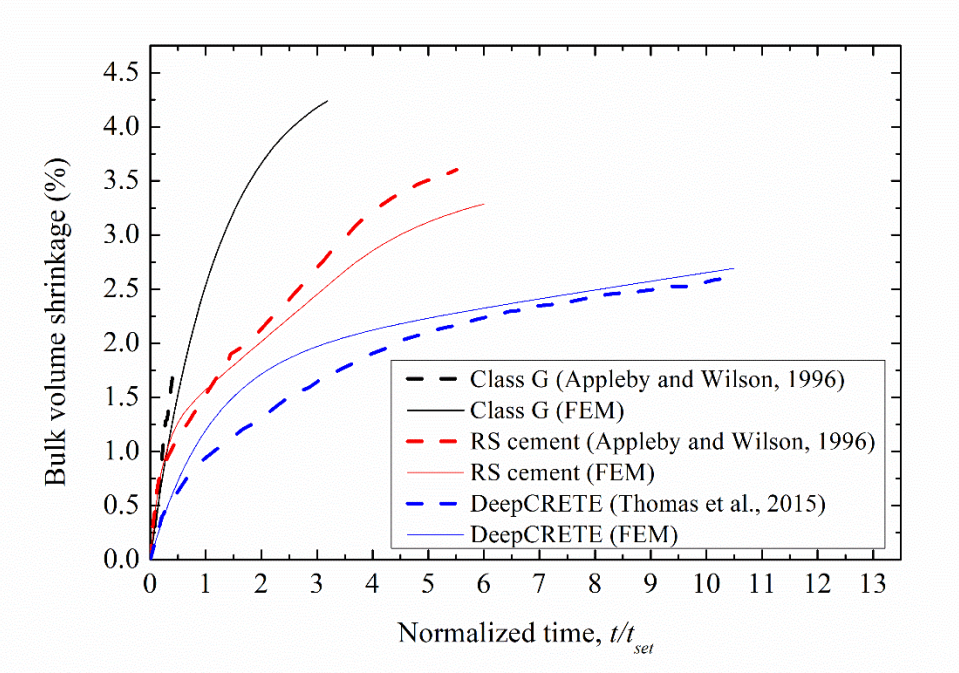

(a)

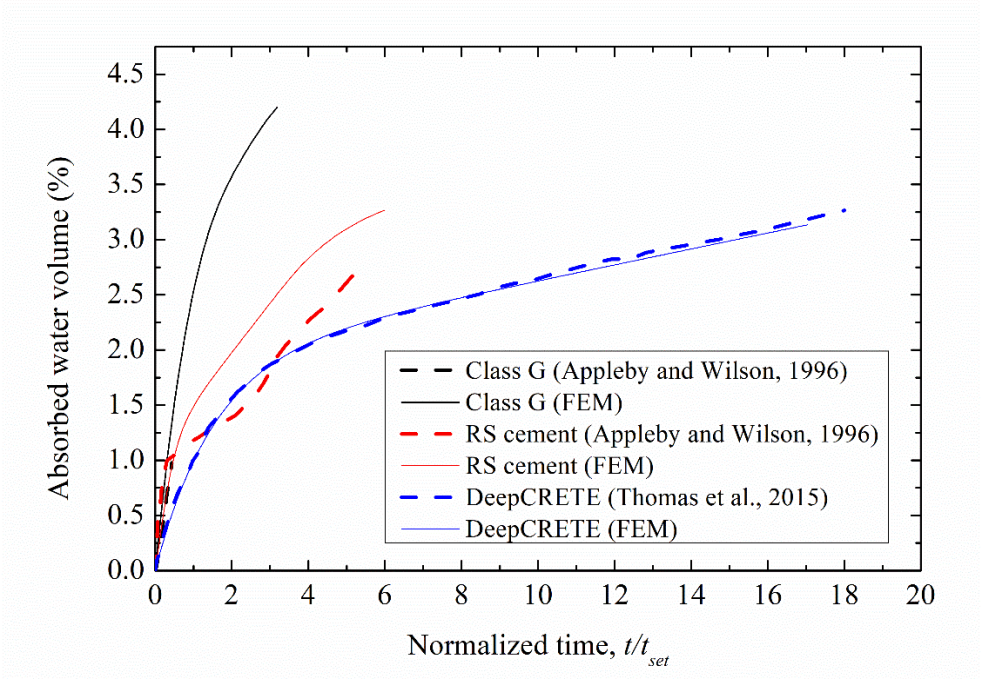

(b)

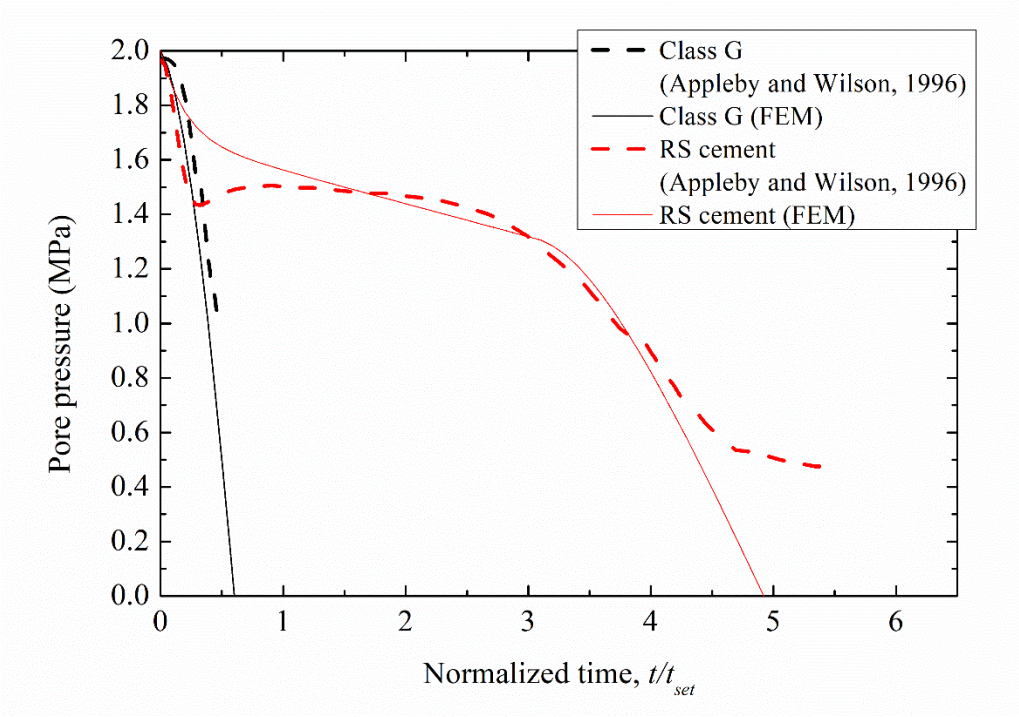

(c)

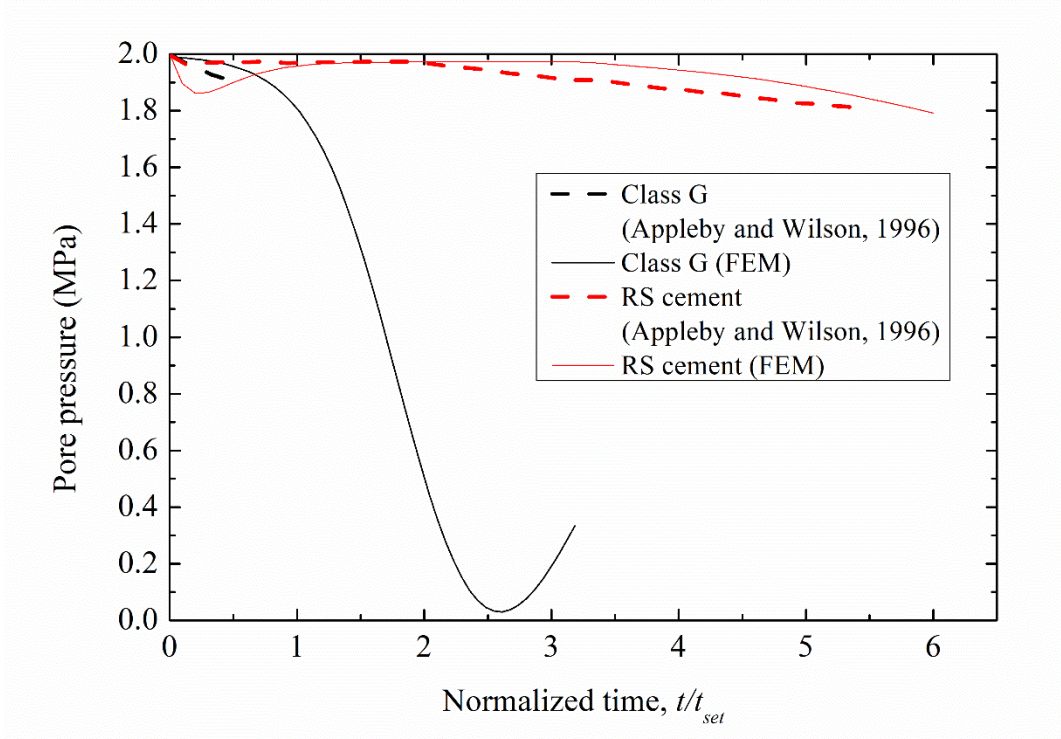

(d)

Figure 4 Finite element model (FEM) calibration results of the laboratory tests on cement shrinkage: (a) bulk shrinkage volume; (b) absorbed water volume; (c) pore pressure (drainage

valve closed); (d) pore pressure (drainage valve open). t_{set} = 7.85 h and 5.0 h for the Class G and RS cement tests, respectively, while t_{set} = 12.0 h and 8.8 h for the bulk shrinkage volume and absorbed water volume of the OPSD cement test, respectively.

3.4 Effect of temperature

The temperature change of cement during hydration may have affected the experimental results through the thermal expansion of cement particles and pore water. To investigate this issue, a semi-coupled thermo-hydro-mechanical simulation was conducted with the FEM shown in Figure 2b. In this simulation, the temperature of cement was calculated by an independent thermal conduction analysis using the laboratory measured heat rate of OPSD slurry as shown in Figure 5. The axi-symmetric eight-node biquadratic displacement, bilinear temperature element was used. The employed thermal properties are shown in Table 3. Because thermal properties of OPSD slurry are not reported, two different values of thermal conductivity were assigned. A reasonable value of the thermal conductivity of Portland cement would be 1.0W/m/K (Zhen & Xiong 2013) (the upper bound). However, OPSD cement contains hollow fly ash particles, which may decrease the bulk thermal conductivity by a couple of orders of magnitude. As the thermal conductivity of air is about 0.025 W/m/K at12ºC, this value is used as the lower bound. The specific heat capacity was assigned as 1.0 J/g/K because the values for Portland cement (Zhen & Xiong 2013) and air are similar to this input value. The thermal expansion coefficient of early-age cement varies with moisture content (Sellevold & Bjøntegaard 2006) and temperature (Cruz & Gillen 1980). In this study, a constant value of 10 με/ºC, which is the mean value of oil well cements (Loiseau 2014), was employed. The model also considered the temperature-dependent thermal expansion coefficient of pore water $(13.41T\text{-}3717)/10^6$ (1/K)). Because the laboratory test was conducted at a constant temperature of 12ºC, the initial temperature was set to 12ºC and the temperature on the model boundaries was specified to a constant value of 12ºC. The simulation period was 160 h.

Results from the thermal analysis of the OPSD cement test are shown in Figure 6. The maximum average temperature increase is 2.3ºC with the lower bound thermal conduction coefficient (i.e. 0.025W/m/K) and is less than 0.1ºC with the upper bound value (i.e. 1.0W/m/K). The computed temperature distributions are fed into the coupled hydro-mechanical simulation. Figure 7 shows that the effect of temperature change (up to 2ºC increase) on the water absorption and shrinkage behaviour of OPSD cement is negligible. During the Class G and RS cement tests (Appleby & Wilson 1996), the maximum temperature changes were measured to be roughly 2ºC, which is similar to the value computed for this OPSD cement case. Based on this finding, the effect of temperature change on water absorption and shrinkage behaviour is assumed to be insignificant.

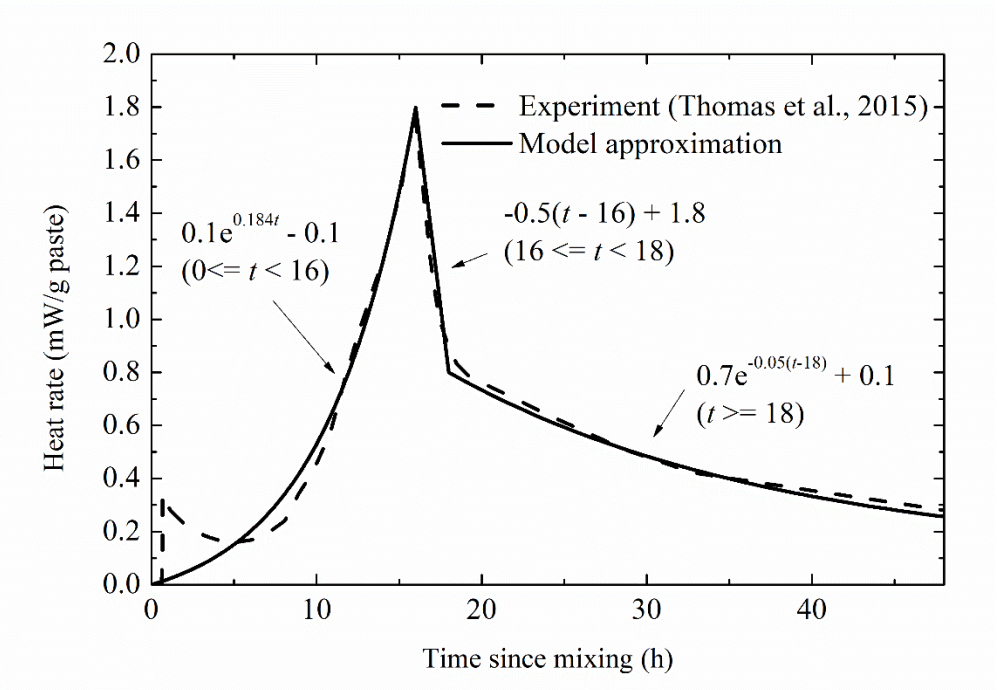

Figure 5 Hydration heat rate of OPSD slurry measured at 12ºC and ambient pressure (Thomas et al. 2015) and its numerical approximation by three curves.

Table 3 Thermal properties of cement, formation and pore water assigned to the FEM.

Thermal conductivity of cement	1.0, 0.025 W/m/K
Thermal conductivity of formation	2.0 W/m/K
Specific heat capacity of cement	1.0 J/g/K
Specific heat capacity of formation	2.0 J/g/K
Thermal expansion coefficient of cement	10 με/K
Thermal expansion coefficient of formation	1.77 με /K
Thermal expansion coefficient of pore water	13.41*T*-3717 με /K

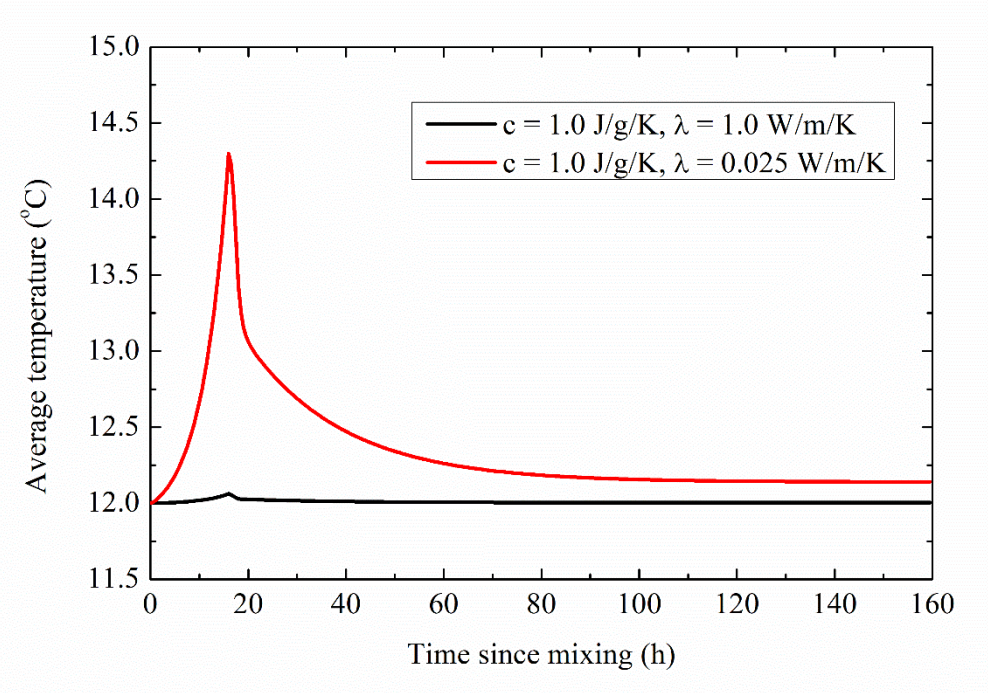

(a)

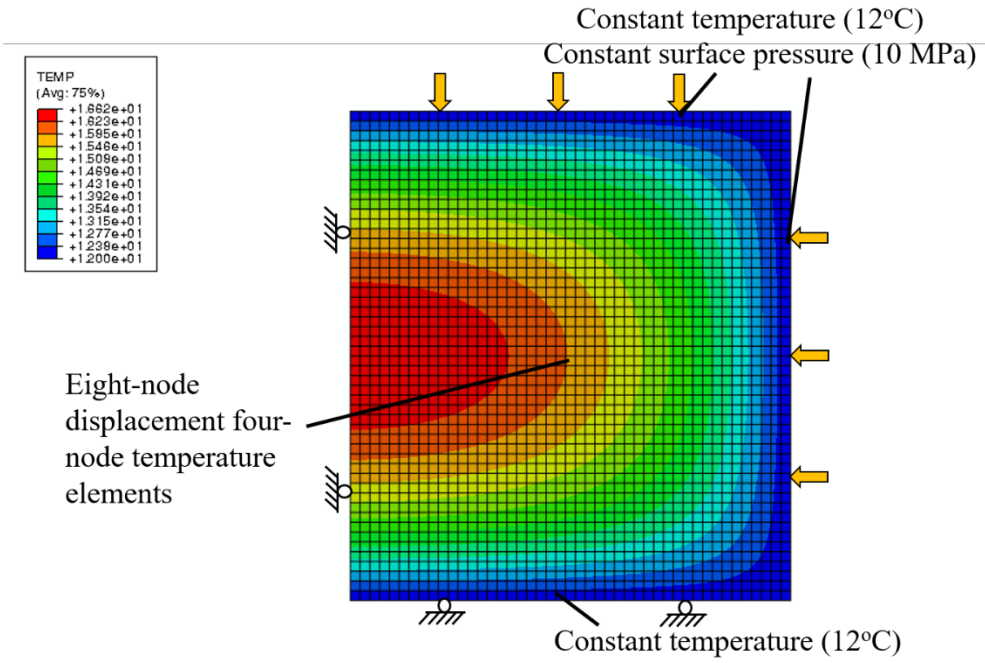

(b)

Figure 6 Results of the thermal analysis on OPSD slurry: (a) average cement temperatures; (b) spatial distribution of cement temperature at 16 h (c = 1.0 J/g/K and λ = 0.025 W/m/K).

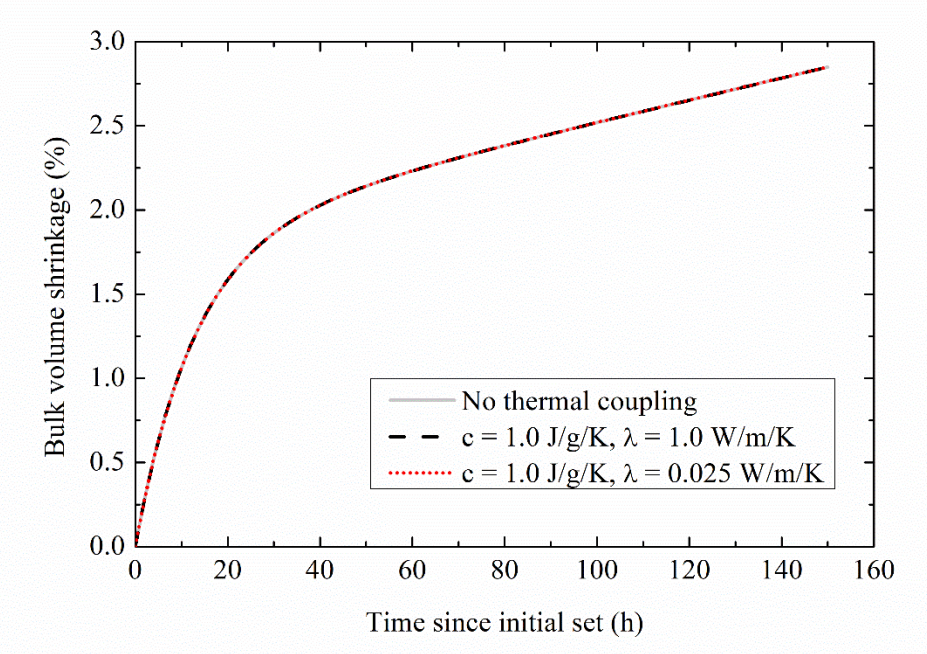

(a)

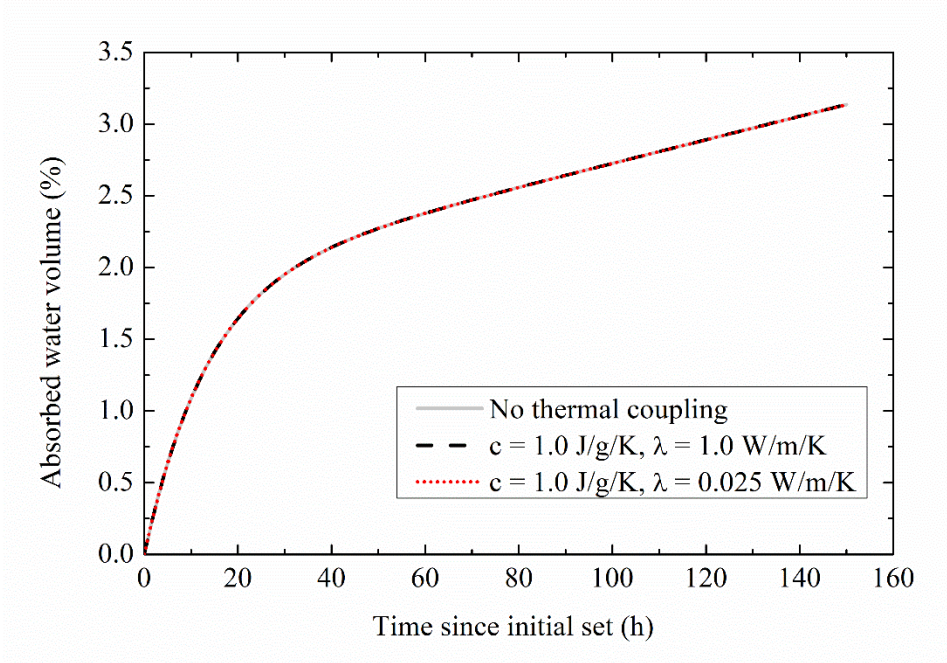

(b)

Figure 7 Results of the coupled hydro-mechanical cement shrinkage analysis of the OPSD cement with different temperature inputs from the thermal analysis: (a) bulk shrinkage volume; (b) absorbed water volume.

4 Modelling of cement shrinkage in a wellbore annulus

4.1 Model dimensions and material parameters

The dimensions of the axi-symmetric FEM are shown in Figure 8. The model represents a thin layer of cement and formation, which are assumed to be located at 100 m below the seafloor at the Nankai Trough in Japan (Yamamoto et al. 2014). The water depth of the seafloor is 1002 m. The inner and outer radius of the cement is set to 0.122 m and 0.156 m, corresponding to the outer diameter of the 9 5/8-in. casing and the diameter of a 12 1/4-in. borehole, respectively. The radial length of the formation model is set to 10m. For both cement and formation, no vertical displacement is allowed (i.e., plane strain condition), assuming radial deformation is dominant.

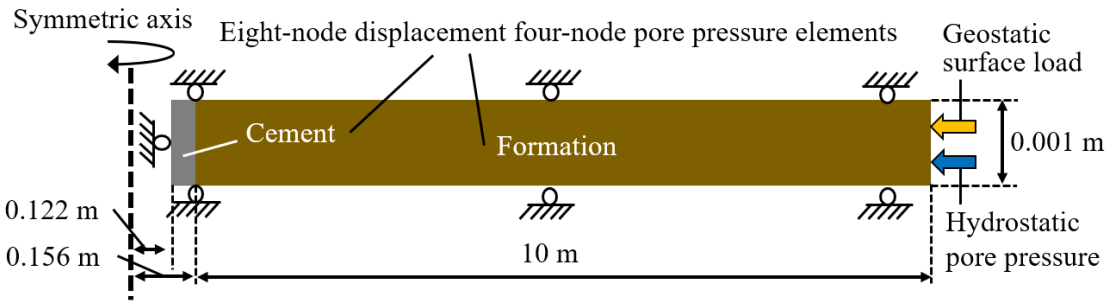

Figure 8 The dimensions of the axi-symmetric FEM for the wellbore model simulation.

Table 4 Material properties of the cement and formation.

	Cement	Formation
Sink rate	Figure 3a	N/A
Permeability	Figure 3b	1 mD-0.1 μD
Young's modulus	Figure 3c	N/A
Swelling gradient	N/A	0.03
Poisson's ratio	0.20	0.25
Porosity	0.25	0.57
Bulk modulus of solid phase	21 GPa	Incompressible
Bulk modulus of fluid phase	2.2 GPa	Incompressible

The ABAQUS finite element software package was employed to carry out the coupled transient fluid flow and stress analysis. The cement and formation are discretised into 20 and 5000 axi-symmetric eight-node biquadratic displacement, bilinear pore pressure elements, respectively. The length and height of each cement element are 1.67 mm and 1 mm, whereas those of each formation element are 2 mm and 1 mm, respectively.

The model properties for the cement and formation are listed in Table 4. For the cement, the incremental linear isotropic elasticity with time-dependent properties evaluated earlier are adopted. The calibrated sink rate, permeability, and Young's modulus (Figure 3) are employed. For the formation, the elastic bulk modulus K is pressure-dependent using Equation 2:

$$K = vp'/\kappa \tag{2}$$

where p' is the mean effective stress, v is the specific volume (=1+e), e is the void ratio and κ is the swelling gradient. A value of κ= 0.03 is used based on the calibration results for this formation (Uchida 2012; Zhou 2015). A constant permeability is assigned to the formation within the range of 1 mD to 0.1 μD as part of parametric study.

4.2 Simulation process

The simulation process was divided into three stages: drilling stage, cement pumping stage, and cement shrinkage stage. The formation and cement were separately modelled in the first two stages, whereas the two were interacting in the final stage.

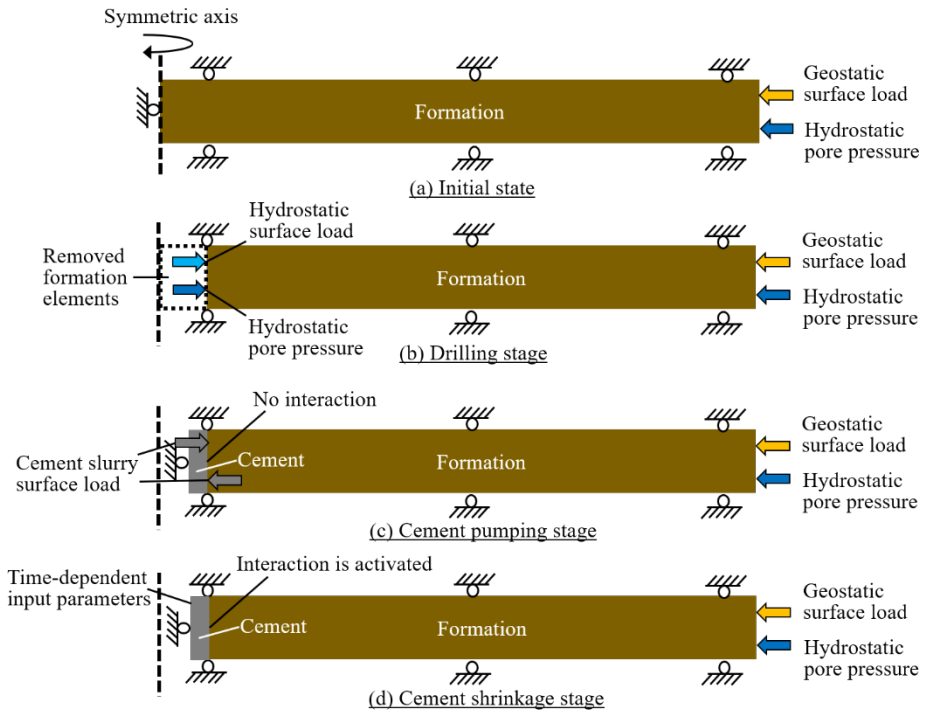

Figure 9 The three-stage process of the wellbore model simulation: (a) initial state; (b) drilling stage; (c) cement pumping stage; (d) cement shrinkage stage

In the initial state (Figure 9a), the cement elements are not active. For the formation, the initial pore pressure and effective stresses are applied to reach geostatic equilibrium. The total vertical stress at a given depth of the Nankai Trough is given by the sum of the weight per unit area of the seawater with the density of 1.030 g/cm^3 and that of the formation with the bulk density of 1.750 g/cm^3 (Suzuki et al. 2015). The vertical effective stress is then calculated by subtracting the hydrostatic pore pressure from the total vertical stress. The initial horizontal effective stress is calculated using Equation 3:

$$\sigma'_h = (1 - \sin\phi')\mathrm{OCR}^{\sin\phi'}\sigma'_v \quad (3)$$

where σ'_h is the horizontal effective stress; σ'_v is the vertical effective stress; ϕ' is the internal effective friction angle of the formation and OCR is the ratio of the past maximum vertical effective stress to the current vertical effective stress. This formula for calculating the horizontal effective stresses is employed in soil mechanics. Because the modelled formation is unconsolidated clayey overburden at the Nankai Trough, this equation is suitable. The internal effective friction angle and OCR value of the Nankai Trough formation is obtained from Nishio et al. (2011). The horizontal pressure corresponding to the initial total horizontal stress of the formation is applied onto the right-hand side boundary of the formation. The pore pressure is fixed to the hydrostatic pressure on the right-hand side boundary, whereas it is free (zero-flux) on the left-hand side boundary.

In the drilling stage (Figure 9b), the formation elements located inside the borehole radius are removed to simulate the drilling process. The surface pressure corresponding to the hydrostatic pressure of seawater is applied on the left-hand side boundary surface. The pore pressure on the left-hand side boundary nodes is specified to hydrostatic seawater pressure to simulate drilling with seawater (i.e. drained condition).

In the cement pumping stage (Figure 9c), the cement elements are activated. The radial displacement on the left-hand side boundary of the cement is constrained to simulate the casing wall. The slurry pressure is applied on the right-hand side surface of the cement. The slurry pressure is evaluated by the weight per unit area of the seawater (1002 m) and cement (100 m). The slurry density used to calculate the slurry pressure is 1900 kg/m^3 for Class G and RS cements and 1200 kg/m^3 for OPSD cement. Two possible scenarios are considered for the initial effective stress and pore pressure. Figure 10a shows one scenario where the effective stress (i.e. interparticle stress) of the cement is zero (σ' = 0) and the entire slurry pressure is converted into

pore pressure ($u = \rho_c gz + p_w$) (i.e. underconsolidated cement case). Figure 10b shows the other scenario where pore pressure becomes the hydrostatic pressure of the formation ($u = \rho_w gz + p_w$) and the effective stress is generated as the difference between the weight of the cement slurry and formation water ($\sigma' = (\rho_c - \rho_w)gz$) (i.e. consolidated cement case). In both cases, the total stress of the cement remains identical to the slurry pressure ($\sigma = \sigma' + u = \rho_c gz + p_w$).

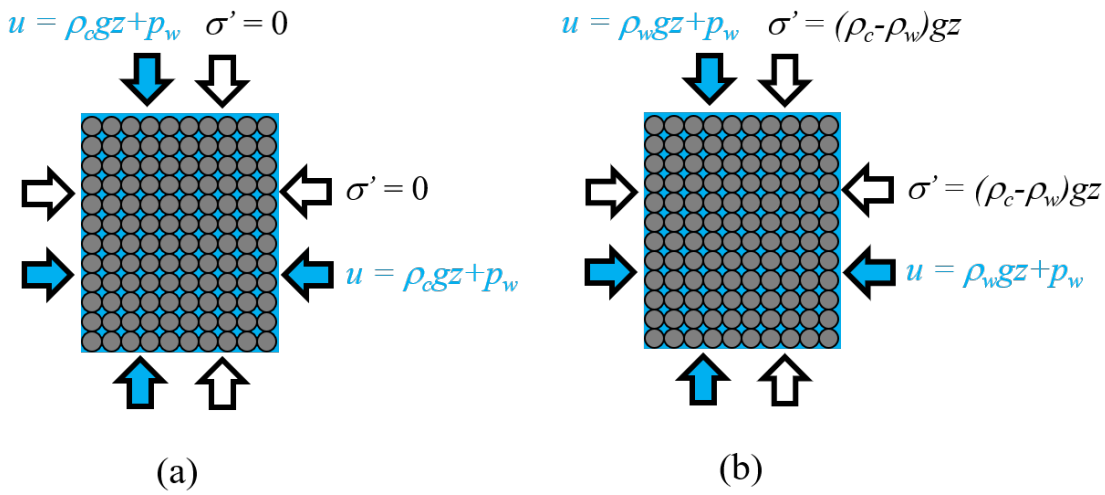

Figure 10 Assumed effective stress and pore pressure of the cement at the onset of cement initial set: (a) underconsolidated cement case; (b) consolidated cement case (σ'=effective stress, u=pore pressure, ρ_c=cement slurry density, ρ_w=water density, g=gravity acceleration, z=depth below seabed, p_w=seawater pressure at seabed).

For the formation, the cement slurry pressure is applied at the left-hand side boundary of the formation, resulting in radial deformation. Zero fluid flux condition is also applied. In response to the total radial stress change, the radial effective stress changes due to the cavity expansion process. The excess pore pressure is zero because the formation is modelled as an isotropic elastic material. Hence the pore pressure remains the same as the initial condition.

In the shrinkage stage (Figure 9d), the surface pressures on the contacting boundaries of the cement and formation are removed and the contact interaction between the right-hand side boundary surface of the cement and the left-hand side boundary surface of the formation is activated. The positions of the corresponding cement and formation nodes are adjusted before the simulation is submitted such that at the onset of the shrinkage stage these nodes are just in contact with each other without penetration or separation. The augmented Lagrange method in ABAQUS is used to enforce the contact interaction between the surfaces. In this contact model, the contact pressure is augmented in direct proportion to the penetration of the surfaces so as to prevent

excessive penetration. No tangential friction is assumed as the vertical displacements of the cement and formation are both specified to be zero. Fluid flow across the contact interface is allowed and pore water moves between the formation and cement. The cement shrinkage is initiated by applying the calibrated time-varying sink rate (Figure 3a), Young's modulus (Figure 3b), and permeability (Figure 3c) to the cement. The period of this stage is set to 150 h with the time increment of 0.5 h.

4.3 Results from the consolidated cement case

When the cement is assumed to be consolidated at the onset of the initial set of cement (i.e. consolidated cement case), the pore pressure in the cement is the same as that of the formation. The pore water movement is therefore governed by the suction pressure development within the cement as well as the permeability contrast between the cement and formation during the hardening process. Figure 11 shows the changes in the absorbed water volume with time for the three cements. The largest absorbed water volume is calculated for Class G cement, whereas it is the lowest for OPSD cement. This trend can be explained by the water-to-cement ratio of each cement, i.e., the lower the ratio the larger the amount of cement particles that reacts and absorbs water. Although the ratios used for Class G and RS cement are not disclosed in Appleby & Wilson (1996), the standard water-to-cement ratio of Class G cement is 0.44. A higher water-to-cement ratio is usually adopted for RS cement as a portion of cement particles is replaced by gypsum to accelerate the initial set (i.e. thickening time). The water-to-cement ratio of OPSD cement is not disclosed in Thomas et al. (2015). However, since hollow fly ash particles represent 50% of the mass of dry ingredients and 41% of total slurry volume, a higher water-to-cement ratio than the other two cements is expected.

For a given cement, the absorbed water volume is in direct proportion to the formation permeability as expected. When the formation permeability is greater than 0.1 mD, the absorbed water volume is the maximum (5.6% for Class G, 4.4% for RS cement and 3.0% for OPSD cement at 150 h). As the formation permeability decreases below 0.1 mD, the absorbed water volume becomes smaller due to limited water supply from the low permeability formation. The absorbed water volume still increases toward the end of the simulated period (150 h) because the asymptotic values of the calibrated sink rates are not zero. Under this condition, the absorbed water volume will keep increasing at a constant rate beyond the simulation period, which is unrealistic. Experimental data sets for longer periods of cement hydration are necessary, with which the sink rate is calibrated to reach zero, to model long-term water absorption behaviours.

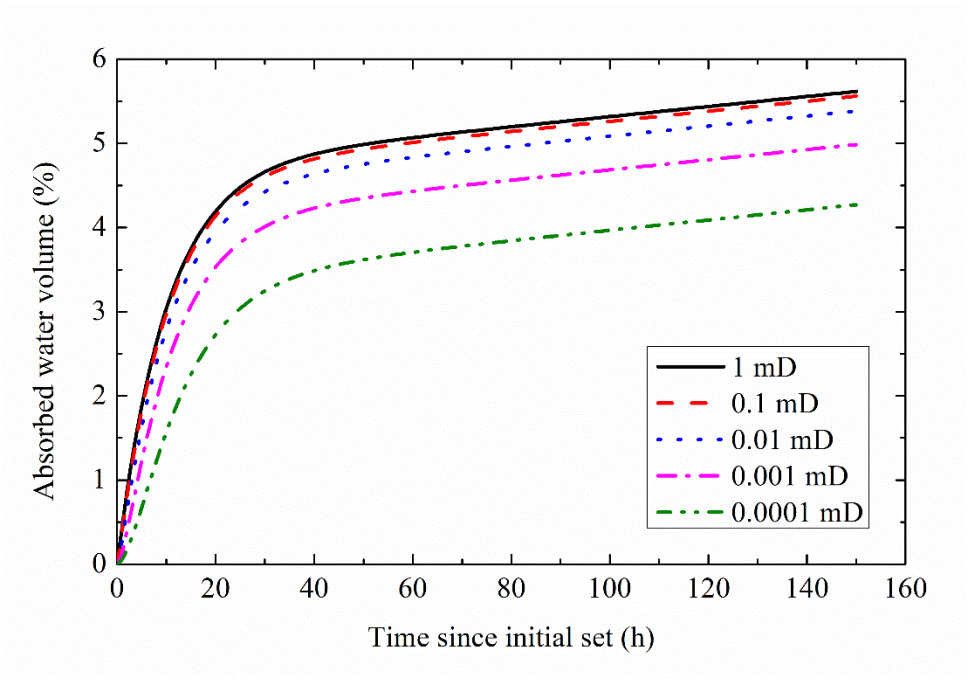
Absorbed water volume (%)
Time since initial set (h)
1 mD
0.1 mD
0.01 mD
0.001 mD
0.0001 mD

(a)

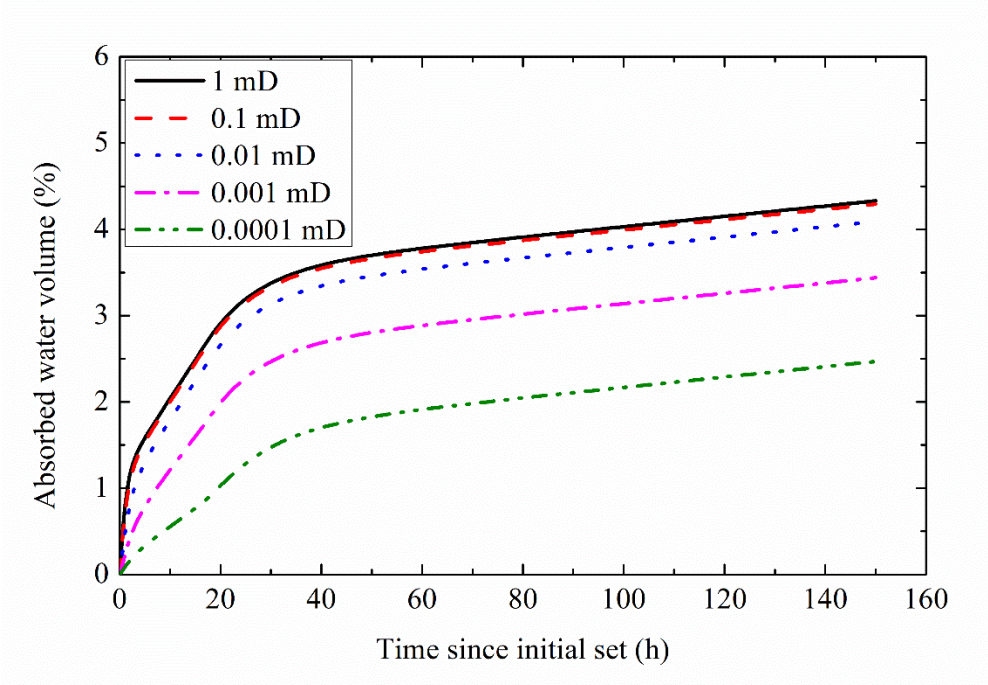
Absorbed water volume (%)
Time since initial set (h)
1 mD
0.1 mD
0.01 mD
0.001 mD
0.0001 mD

(b)

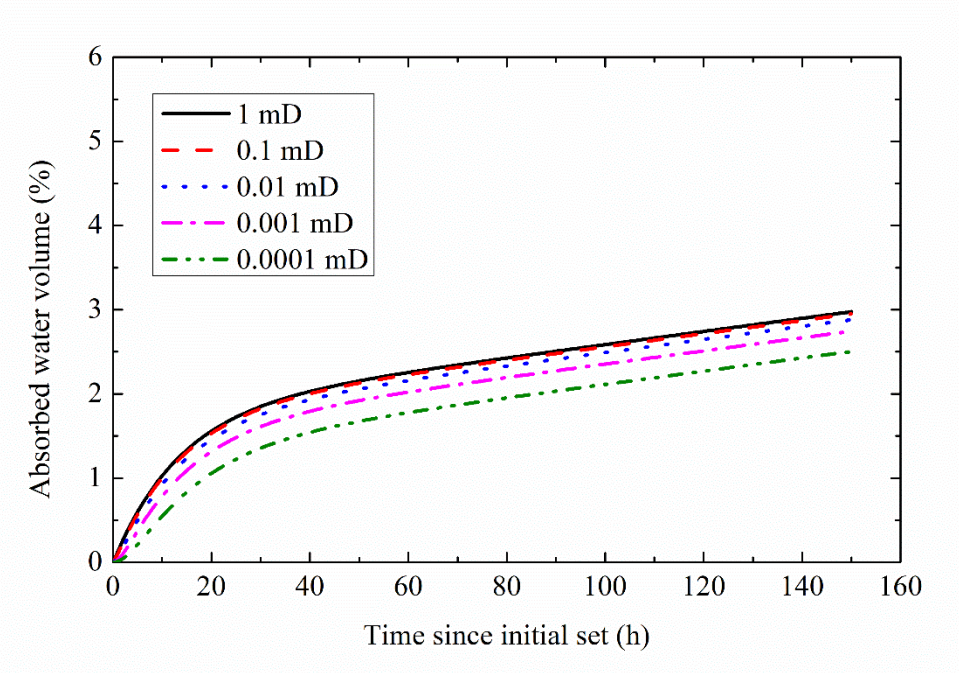

(c)

Figure 11 Absorbed water volume of cements since the initial set in the consolidated cement case: (a) Class G cement; (b) RS cement; (c) OPSD cement.

The computed time-dependent pore pressure in the cement at the contact surface with casing is given in Figure 12 for different formation permeability values and different cements. When the formation permeability is greater than 0.1 mD, the pore pressure remains close to hydrostatic. However, as the formation permeability decreases, the pore pressure reduces due to suction pressure developing in the cement during the initial hydration process. The suction development is greater when water supply from the formation is more restricted. As the hydration continues, the suction pressure development decreases and the cement stiffness increases. Consequently, the pore pressure recovers back to the hydrostatic condition. The pore pressure does not recover to hydrostatic when the formation permeability is lower than 0.01 mD. This is because the cement hydration process continues under restricted water supply from the formation. Pore pressure is stabilized below hydrostatic as the cement suction pressure is balanced with the limited water supply from the formation. In a long term, it is expected that pore pressure will go back to the hydrostatic pressure. To model such pore pressure change, experimental data sets for longer periods of cement hydration are necessary.

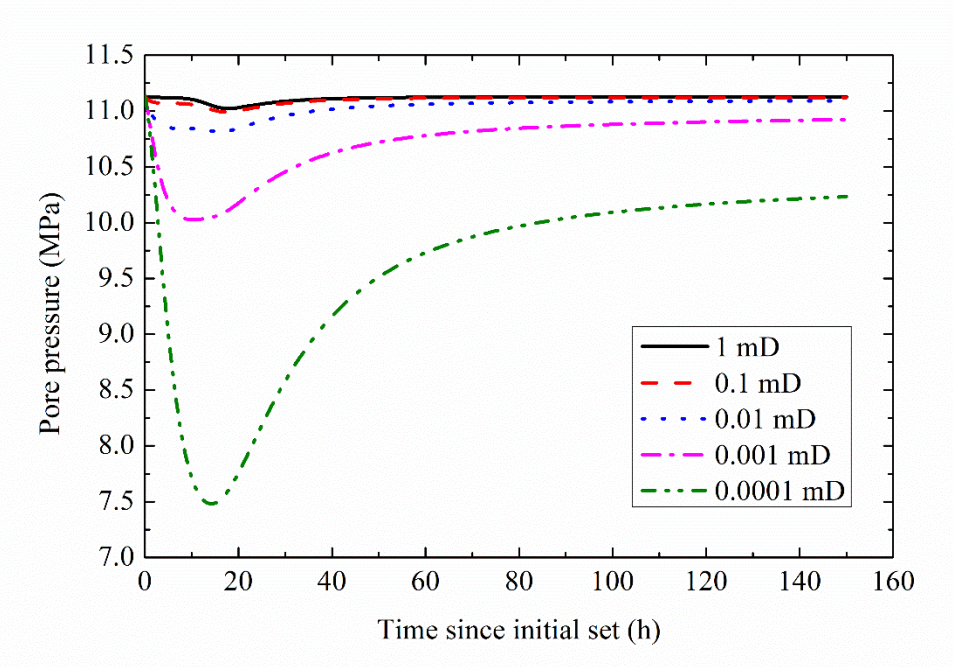
Pore pressure (MPa)
Time since initial set (h)
1 mD
0.1 mD
0.01 mD
0.001 mD
0.0001 mD

(a)

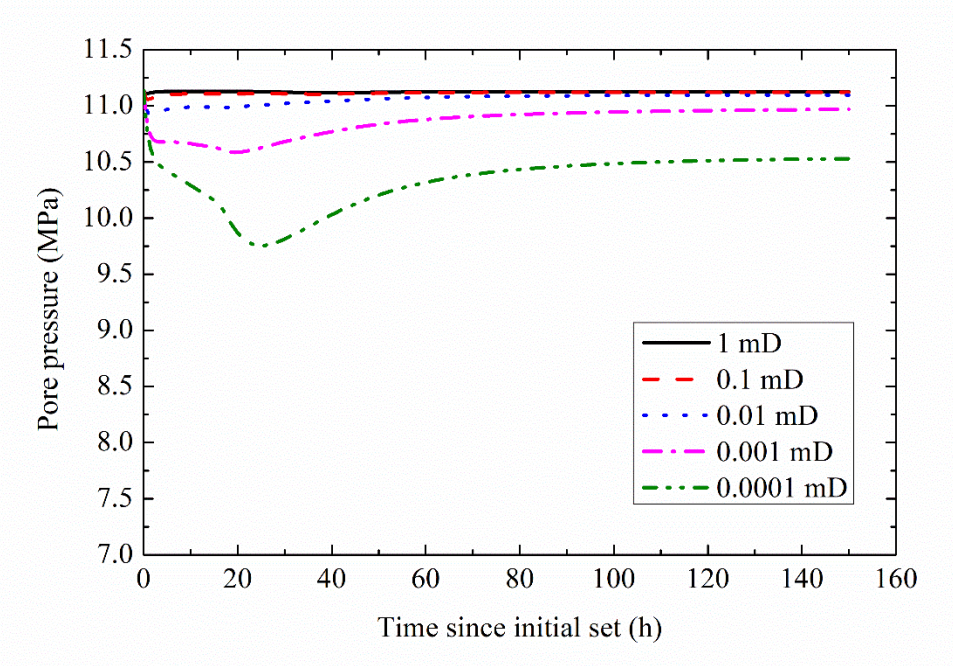
Pore pressure (MPa)
Time since initial set (h)
1 mD
0.1 mD
0.01 mD
0.001 mD
0.0001 mD

(b)

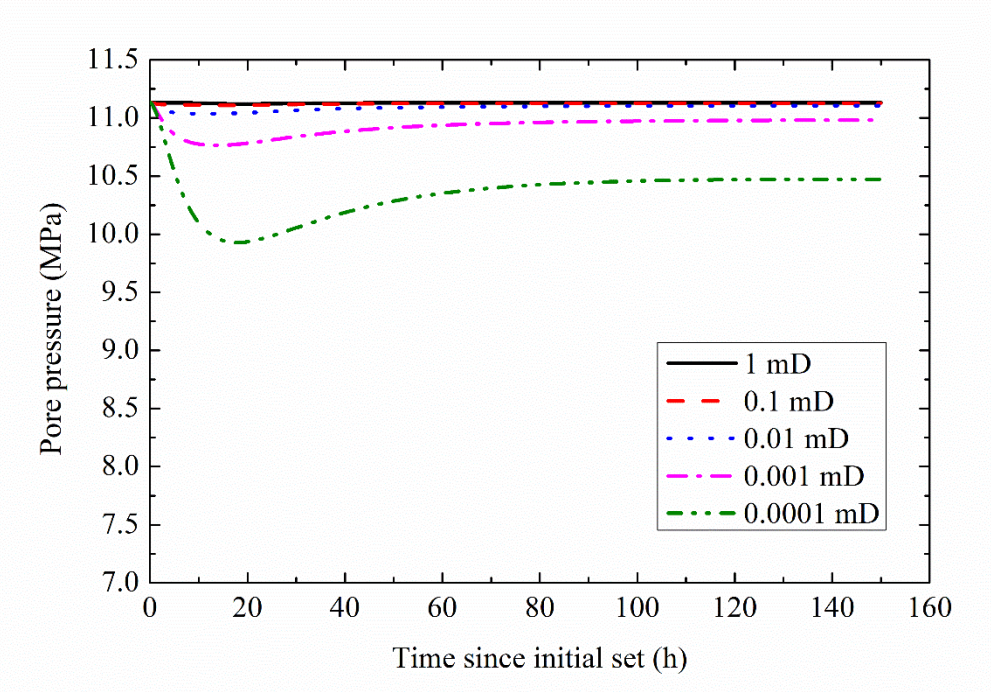

(c)

Figure 12 Pore pressure decrease in cements in the consolidated cement case at the contact surface with casing since the initial set: (a) Class G cement; (b) RS cement; (c) OPSD cement.

The bulk shrinkage behaviour with time is shown in Figure 13. When the formation permeability is greater than the threshold value of 0.1 mD, the amount of shrinkage is very small because the cement is absorbing water from the surrounding formation during hydration. The amount of shrinkage increases as the formation permeability decreases and the amount of absorbed water during hydration decreases. The total shrinkage volume under the formation permeability of 0.1 μD is 1.3%, 1.8%, and 0.5% for Class G cement, RS cement, and OPSD cement, respectively. The behaviour of RS cement shows initial shrinkage immediately after the initial set but then swells back with time when the formation permeability is greater than 0.01 mD. This is because of the large initial sink rate of RS cement, which generates large temporal pore pressure decrease. However, the pore pressure quickly recovers by the flow of formation pore water into the cement. When the permeability is less than 0.01 mD, the flow from the formation is not fast enough and shrinkage increases with time. In all cases, the shrinkage process completes after certain time even though the absorbed water volume and pore pressure keep changing. This is because stiffness values of the cements become high enough that any additional cement volume change by any pore pressure change is negligible.

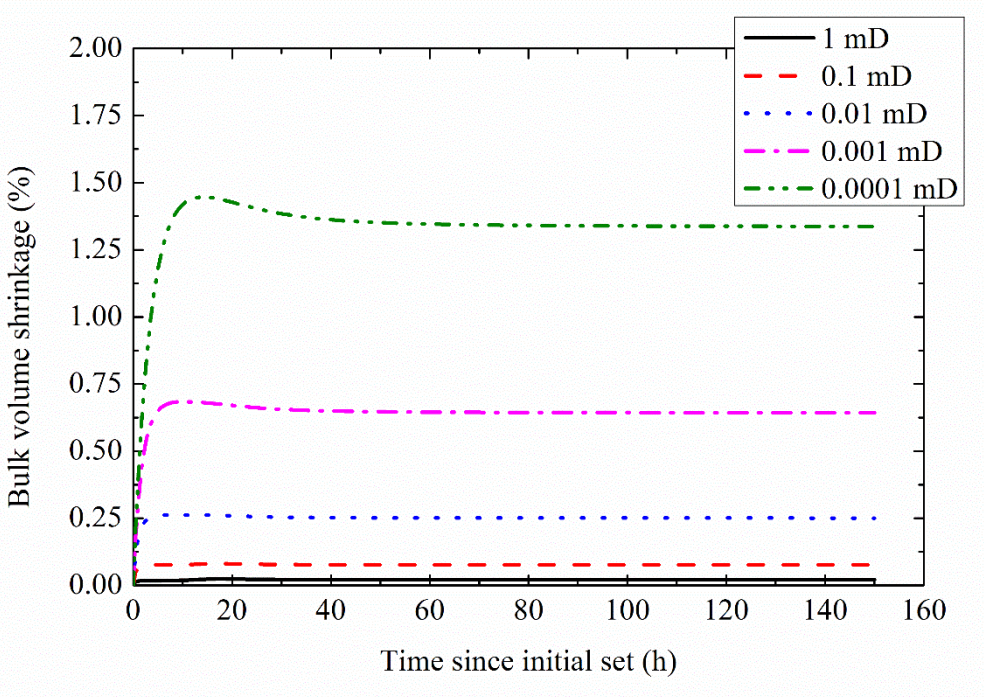
1 mD
0.1 mD
0.01 mD
0.001 mD
0.0001 mD
Bulk volume shrinkage (%)
Time since initial set (h)
0.00
0.25
0.50
0.75
1.00
1.25
1.50
1.75
2.00
0
20
40
60
80
100
120
140
160

(a)

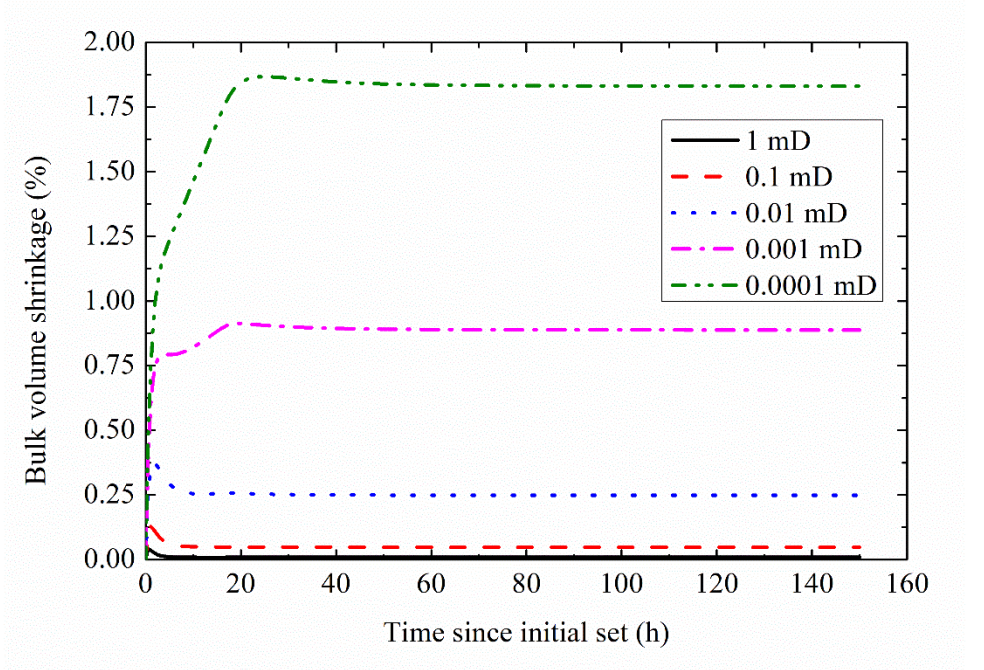
1 mD
0.1 mD
0.01 mD
0.001 mD
0.0001 mD
Bulk volume shrinkage (%)
Time since initial set (h)
0.00
0.25
0.50
0.75
1.00
1.25
1.50
1.75
2.00
0
20
40
60
80
100
120
140
160

(b)

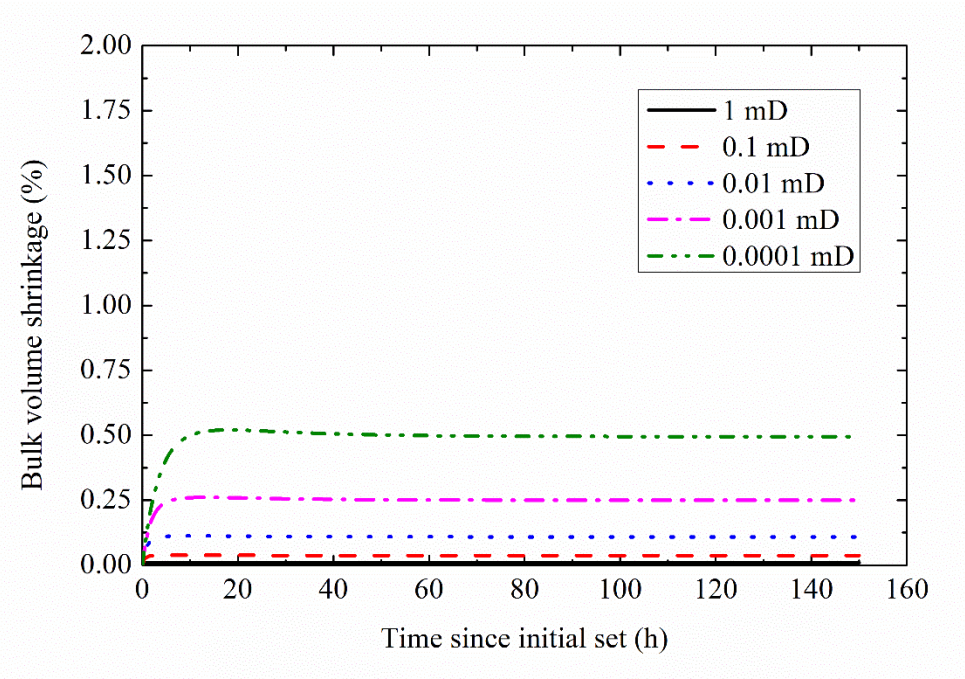

(c)

Figure 13 Bulk shrinkage volume of cements since the initial set in the consolidated cement case: (a) Class G cement; (b) RS cement; (c) OPSD cement.

4.4 Results from the underconsolidated cement case

It is possible that the cement is not consolidated when the initial set of cement occurs. In this section, an extreme case of underconsolidated cement with zero effective stress is considered. Because the pore water in the cement is greater than that of the formation, the water flows from the cement to the formation initially. However, as the cement hydrates, water then starts to flow back into the cement as is observed in the consolidated cement case. Hence, complex water movement is expected in this case.

The computed absorbed water volume changes with time are shown in Figure 14 for the three cements. Different from the consolidated cement case, the amount of absorbed water volume is not in direct proportion to formation permeability. This is because the pressure difference across the cement-formation interface causes the outflux of cement pore water, resulting in negative values of absorbed water volume. As the formation permeability increases, the outflux becomes greater. However, as the hydration progress, the cement starts to absorb water from the formation. The water influx to the cement increases with increasing formation permeability. This competing water movement causes complex absorbed water volume changes. For example, in case of Class G cement, the absorbed water volume in the 0.1 mD case is the largest compared to the other

cases with the formation permeability greater or less than 0.1 mD. In case of OPSD cement, the differences in absorbed water volume are small within the cases of different formation permeability values. In reality, the cement would be partially consolidated or the pore pressure of the formation around the cement would be greater than the hydrostatic condition due to infiltration of the slurry into the formation. Thus, the calculated cement pore water outflux may be somewhat exaggerated.

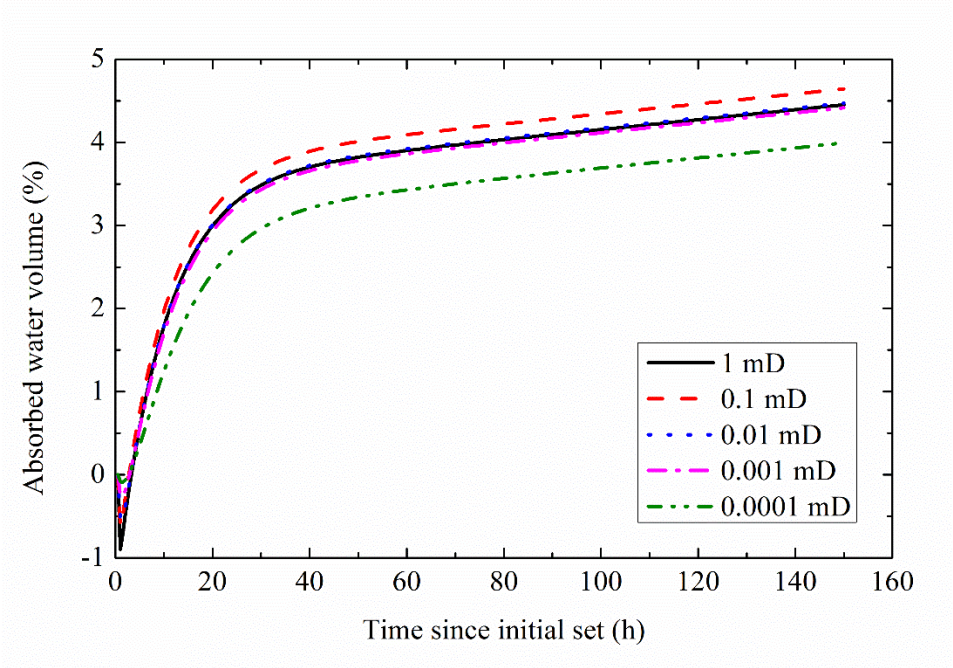

(a)

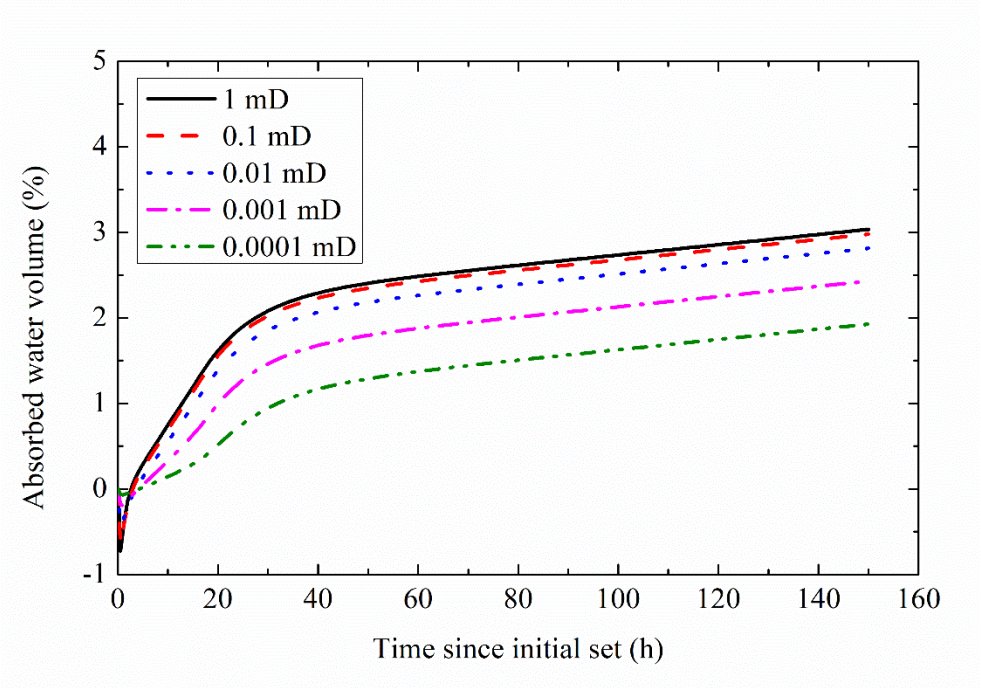

(b)

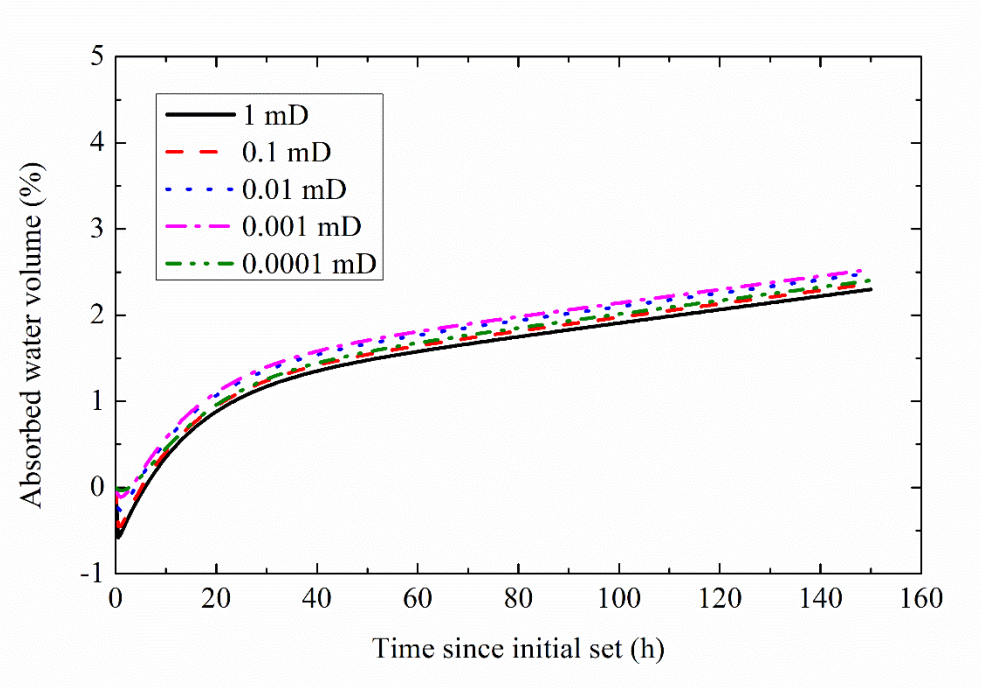

(c)

Figure 14 Absorbed water volume of cements since the initial set in the underconsolidated cement case: (a) Class G cement; (b) RS cement; (c) OPSD cement.

The changes in the cement pore pressure at the interface with casing are shown in Figure 15.

When the formation permeability is greater than 0.1 mD, the pore pressure decreases to the formation pressure of 11.14 MPa at the initial stage of hydration. When the formation permeability is less than 0.1 mD, the pore pressure decreases further with decrease in formation permeability as capillary suction pressure increases. However, pore pressure recovers back to the hydrostatic state with time as the hydration process progresses. A similar trend is observed in the consolidated cement case.

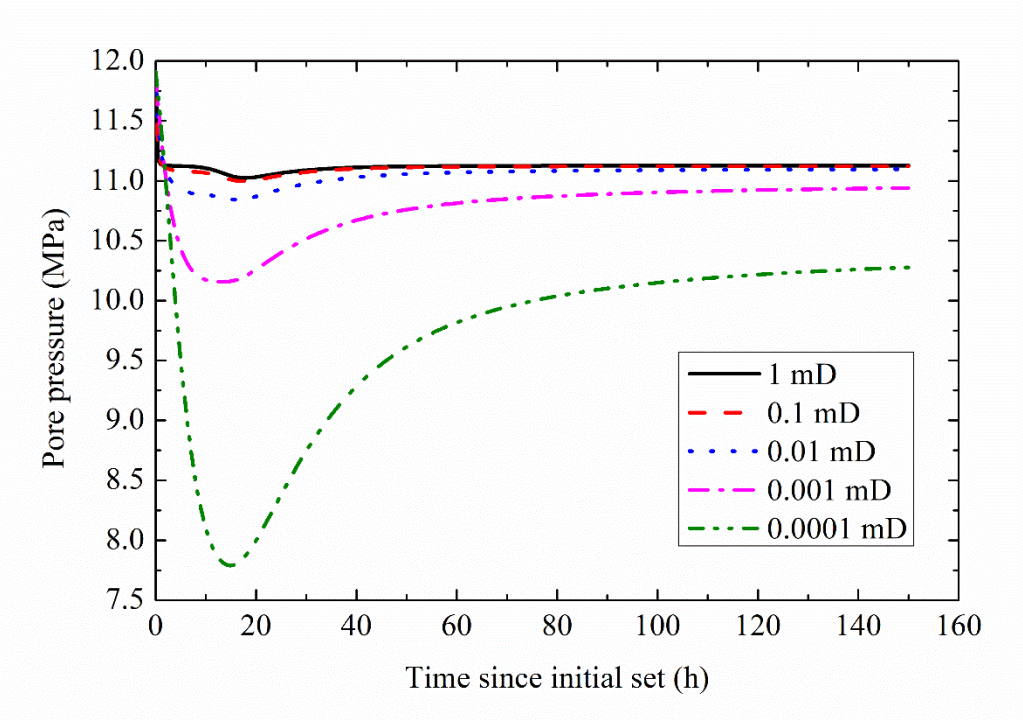

(a)

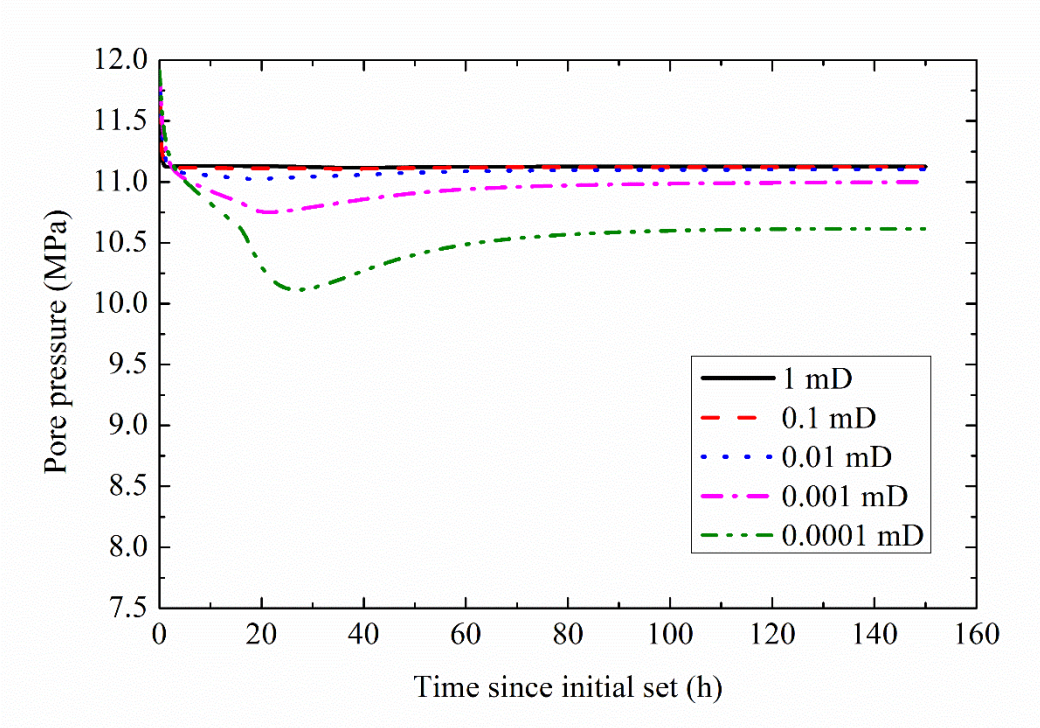

(b)

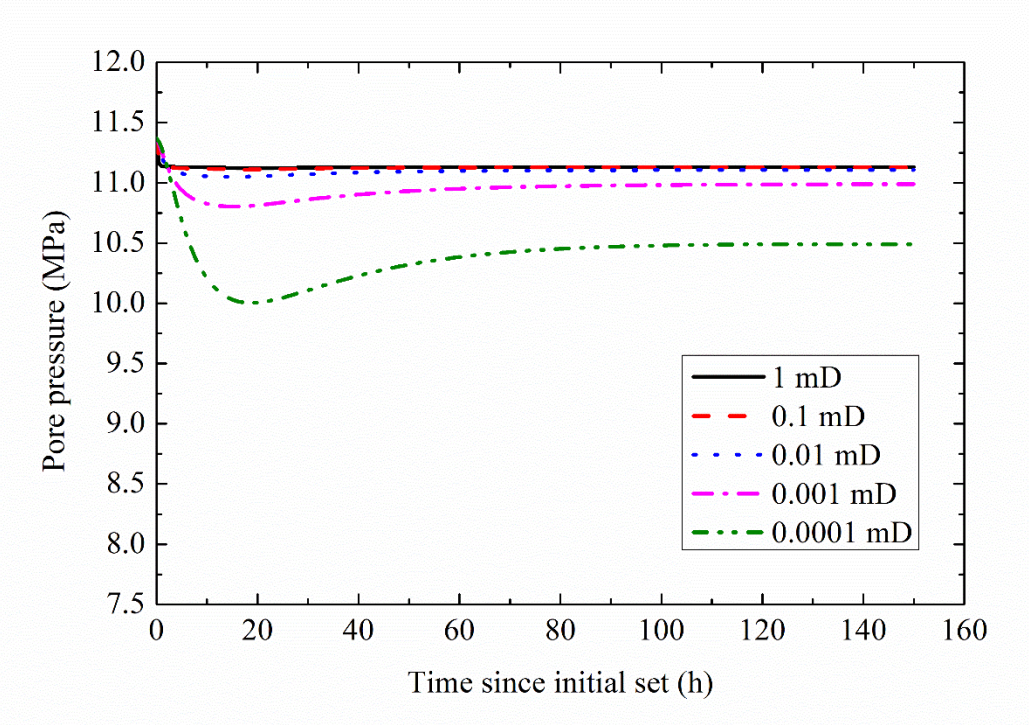

(c)

Figure 15 Pore pressure decrease in the cement at the contact surface with casing since the initial set in the underconsolidated cement case: (a) Class G cement; (b) RS cement; (c) OPSD cement.

Figure 16 shows the bulk shrinkage behaviour of Class G cement, RS cement and OPSD cement, respectively. The trend observed here is inverse to what is observed in absorbed water volume. The total bulk shrinkage volume can be divided into two parts: (i) initial shrinkage due to the outflux of cement pore water and (ii) primary shrinkage due to cement water absorption. The initial shrinkage increases with increasing formation permeability, whereas the primary shrinkage decreases with increasing formation permeability. Because of the opposite trends of the initial shrinkage and primary shrinkage with respect to formation permeability, the total shrinkage does not correlate well with formation permeability.

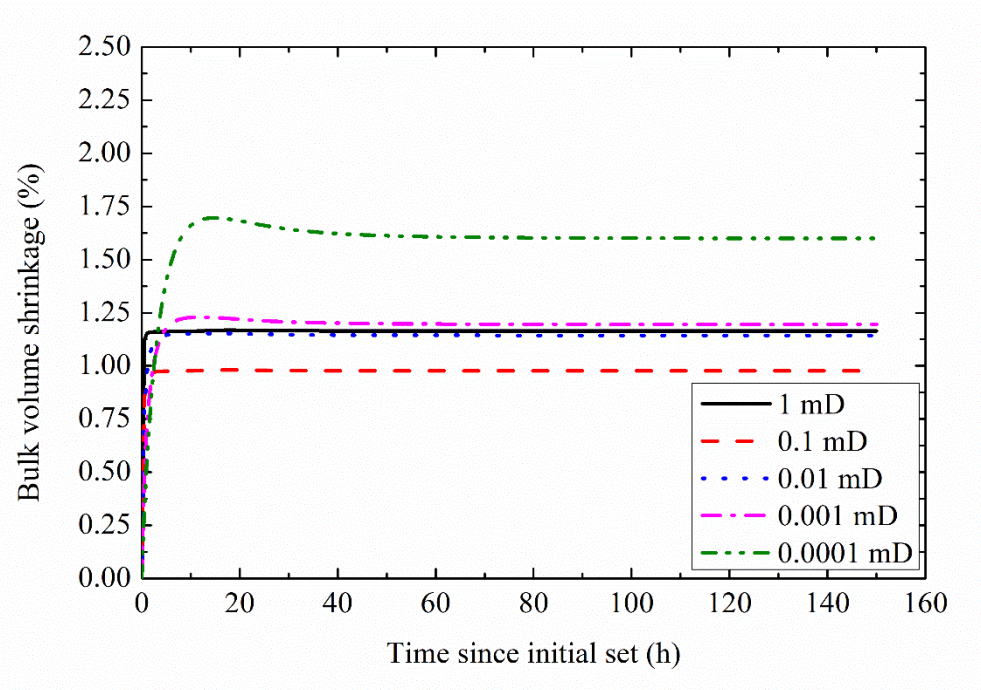

(a)

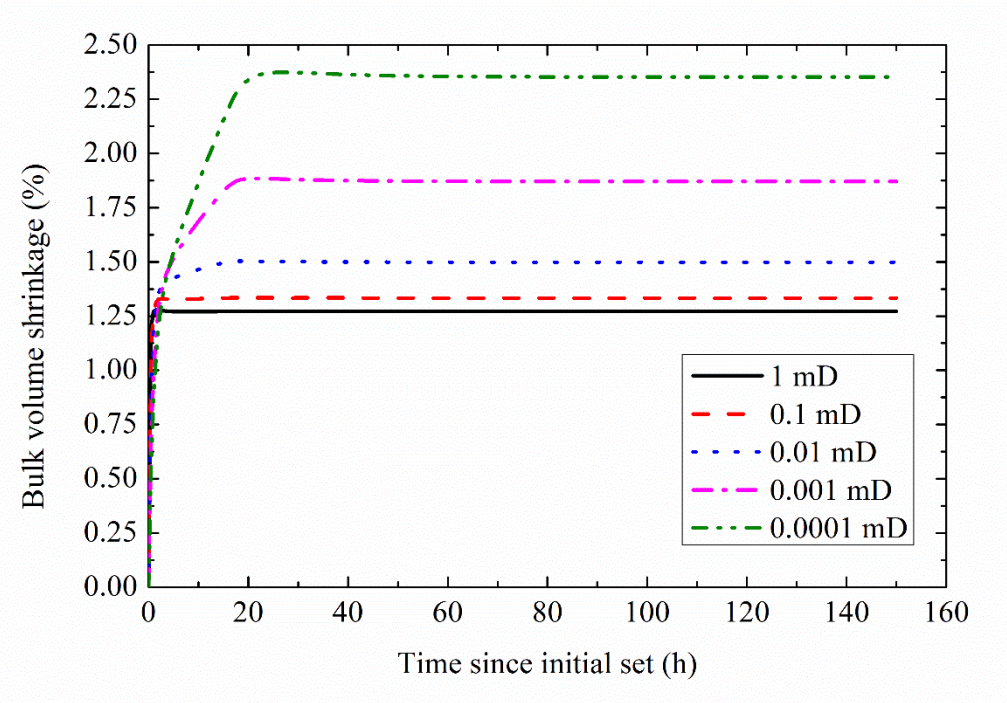

(b)

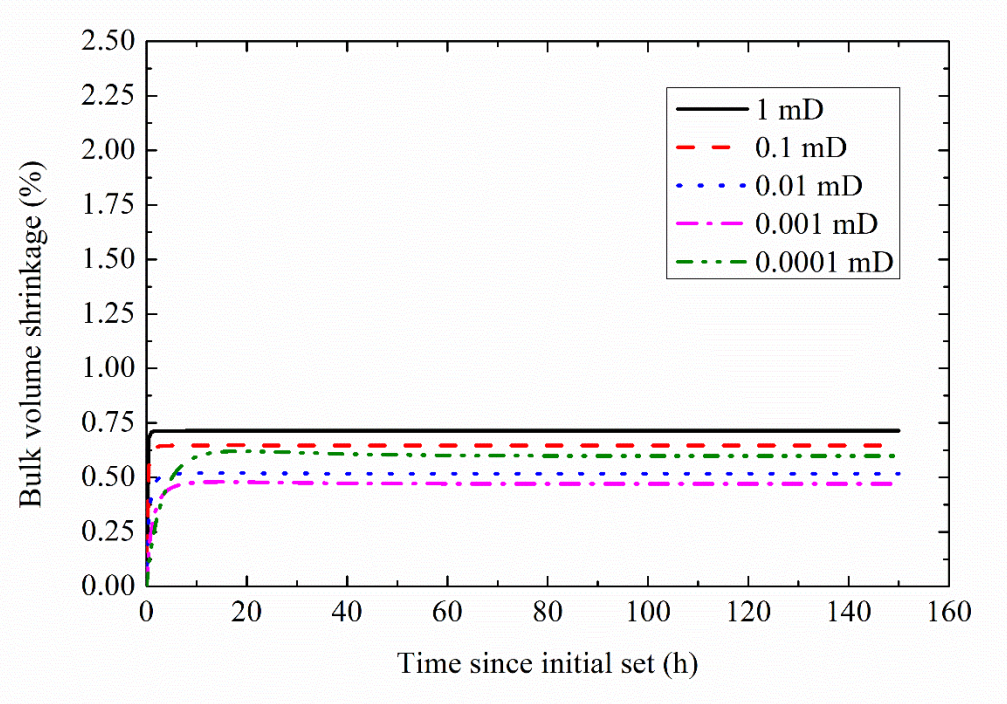

(c)

Figure 16 Bulk shrinkage volume of cements since the initial set in the underconsolidated cement case: (a) Class G cement; (b) RS cement; (c) OPSD cement.

4.5 Effect of cement hydration heat

As was performed for the calibration simulation, a semi-coupled thermo-hydro-mechanical analysis on the water absorption and shrinkage behaviour of the annular cement was carried out to assess the effect of temperature change. First, a thermal analysis was conducted to compute the temperature distribution of the cement. The axi-symmetric eight-node biquadratic displacement, bilinear temperature element was assigned to the identical FEM shown in Figure 8. The thermal properties of the cement (i.e., OPSD cement) and formation are listed in Table 3. The initial temperature was set to 12ºC. The model boundary was specified with a constant temperature of 12ºC. The simulation period was set to 160 h. The computed average temperatures within the cement with time are shown in Figure 17 for two different thermal conductivity values. The temperature increase of the cement is greater in the wellbore configuration compared to the laboratory test configuration. This is because in the wellbore configuration the radial dimension of the cement is larger than that in the laboratory test configuration, and it is also because no thermal conduction in the vertical direction is allowed in the wellbore configuration.

The computed temperatures were applied to the coupled hydro-mechanical simulations. The formation permeability was set to 0.1 μD. The results shown in Figure 18 indicate that the effect of temperature changes on the hydration of OPSD cement on the absorbed water and bulk shrinkage behaviour is found to be insignificant for this wellbore geometry, similar to what was found in the laboratory cases.

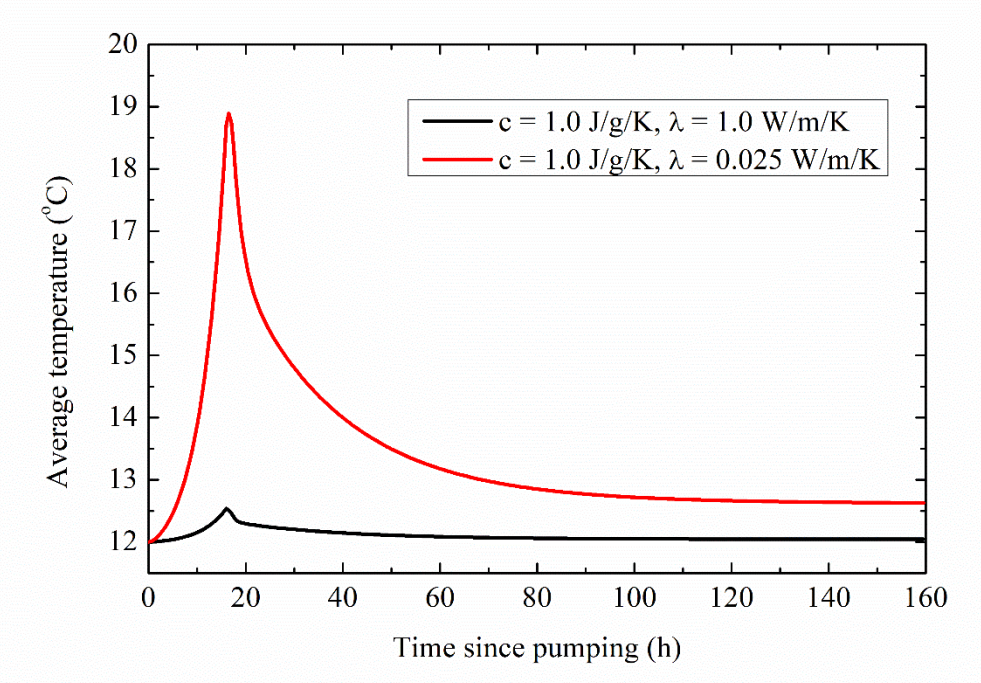

Figure 17 Changes in the average cement temperature of OPSD slurry computed in the thermal analysis in the wellbore configuration.

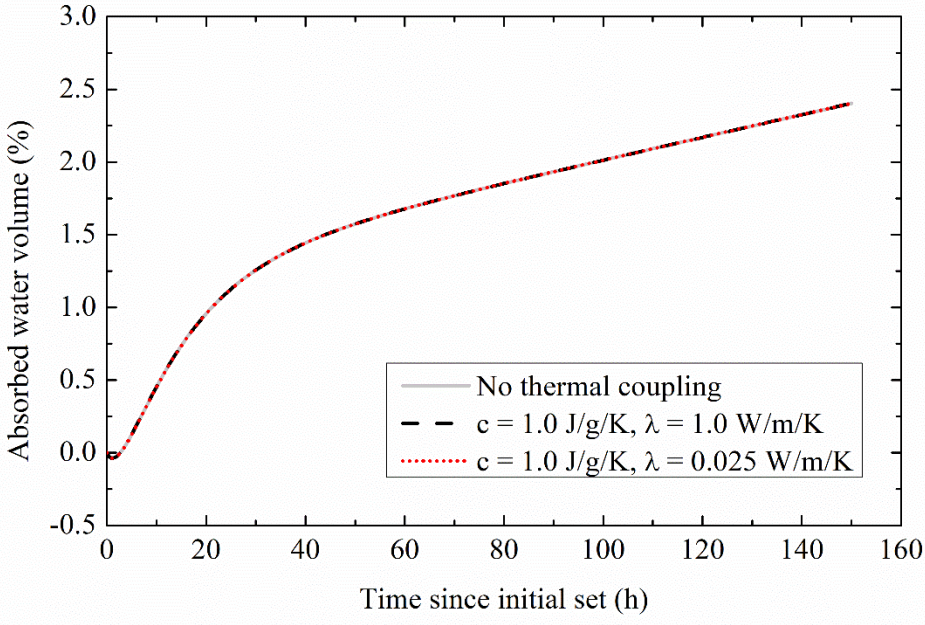

(a)

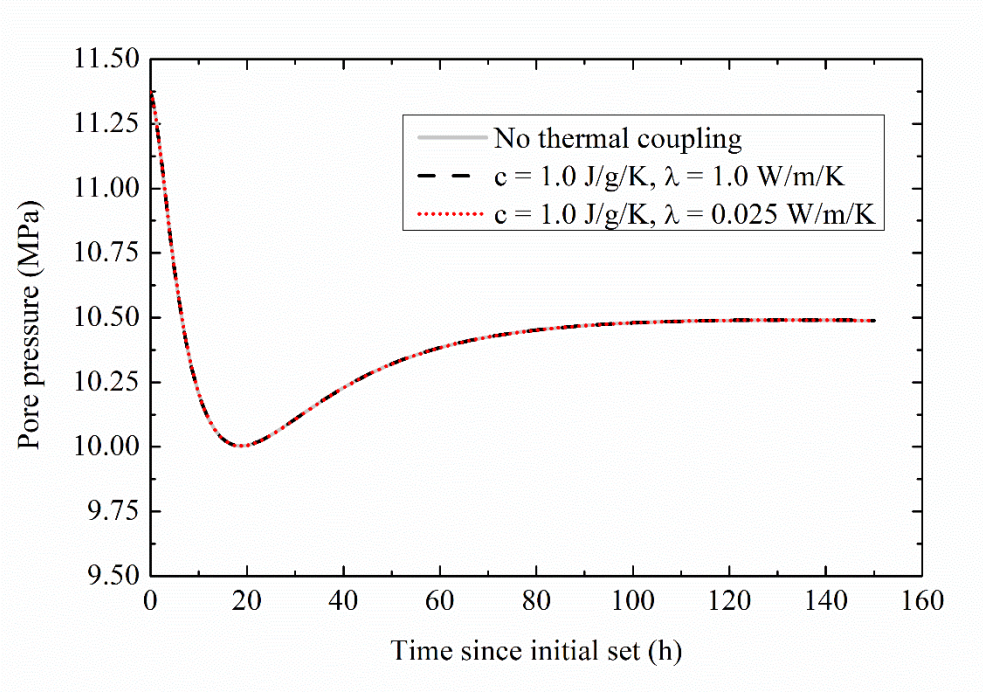

(b)

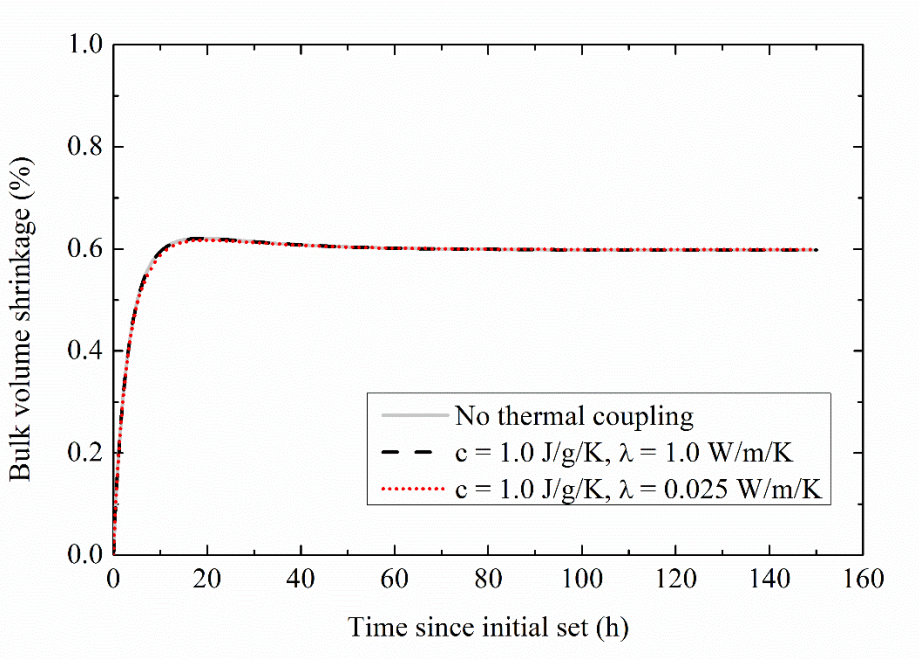

(c)

Figure 18 Result of the semi-coupled thermo-hydro-mechanical analysis on OPSD cement in the wellbore configuration: (a) absorbed water volume; (b) pore pressure; (c) bulk shrinkage volume.

4.6 Discussion

Figure 19 shows the correlation between cement bulk shrinkage volume at the end of the

simulation period (150 h) and formation permeability for both consolidated and underconsolidated cement cases. In the consolidated cement case (Figure 19a), shrinkage values monotonically increase as formation permeability decreases. When formation permeability is greater than 0.1 mD, cement bulk shrinkage volume is smaller than 0.08% for the three cements. As formation permeability decreases below this value, bulk shrinkage of cements increases significantly. In the underconsolidated cement case (Figure 19b), bulk shrinkage volume does not necessarily increase monotonically with decreasing formation permeability due to the competing initial and primary bulk shrinkage volume trends with respect to formation permeability explained in the previous section. The bulk shrinkage volume of cements is greater than 0.6% even when formation permeability is above 0.1 mD. The larger shrinkage values than those in the consolidated cement case are calculated due to the initial outflux of cement pore water into the formation (i.e. initial shrinkage).

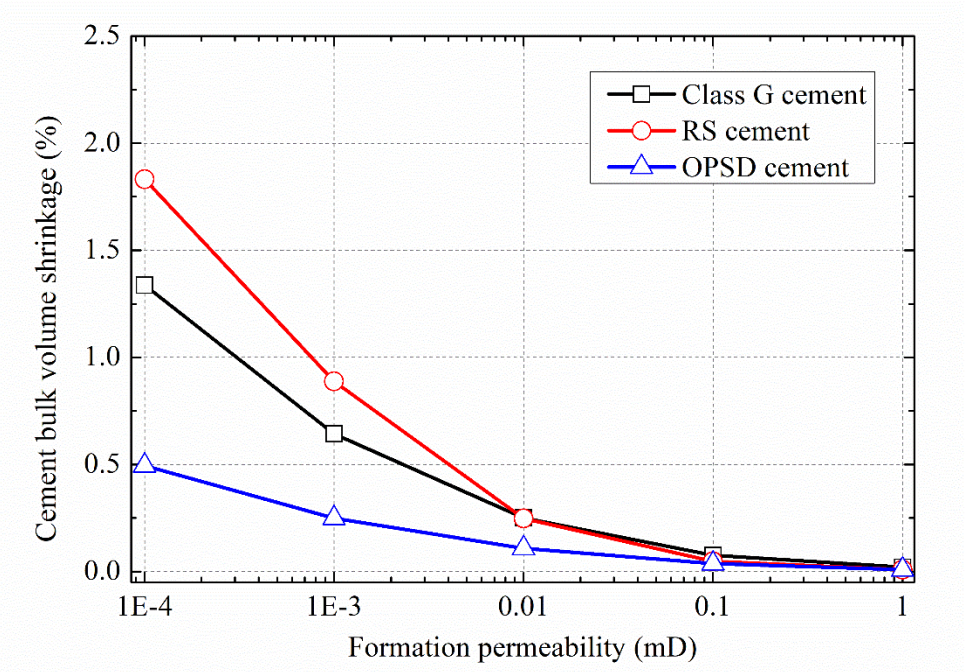

(a)

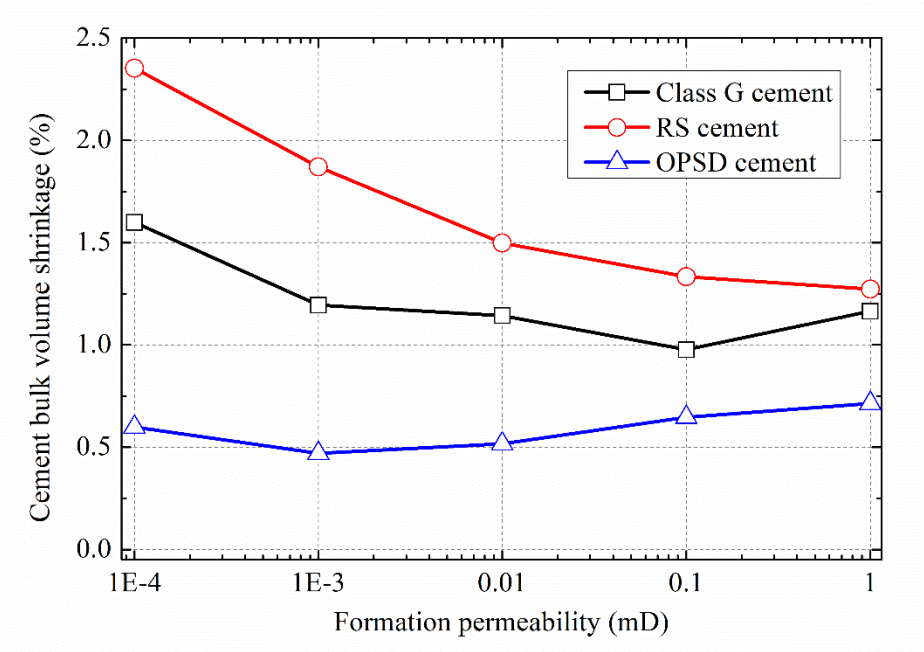

(b)

Figure 19 Correlations between bulk shrinkage volume of cements at 150 h and formation permeability: (a) consolidated cement case; (b) underconsolidated cement case.

For the well geometry considered in this study, the threshold formation permeability, above which the provision of sufficient water into the cement is guaranteed, appears to be 0.1 mD for both consolidated and underconsolidated cases. The minimum permeability in the methane hydrate concentrated layer of the Nankai Trough is 0.01 mD based on the formation core analysis (Konno et al. 2015) and wireline logging data (Fujii et al. 2015). Therefore, water provision to the hardening cement would be limited near the reservoir layer. In addition, the overburden is composed of clayey formation, which would have permeability lower than 0.01 mD. In this case, insufficient water provision to the cement could cause larger-than-expected cement shrinkage volume. When a formation has a permeability of 0.01 mD, the computed total shrinkage volume at 150 h in the consolidated case (underconsolidated case) is 0.25% (1.1%), 0.25% (1.5%), and 0.11% (0.52%) for Class G cement, RS cement and OPSD cement, respectively.

It is noted that the temperature and pressure conditions in the actual wellbore are different from those of the laboratory shrinkage test for Class G and RS cements. In the actual wellbore, typical temperature and pressure are about 12°C and 12 MPa (Yamamoto et al. 2017), whereas the laboratory shrinkage test, whose data were used for model calibration, was conducted at approximately 20°C and 2 MPa. The literature shows that cement shrinkage volume becomes greater when the temperature and pressure increases (Backe et al. 1998; Reddy et al. 2009). Hence

the amount of shrinkage volume might be underestimated for Class G and RS cement. Moreover, one of the modelling assumptions is that the formation remains poro-elastic. In reality, the stress distribution in the formation near the wellbore could be more complex due to soil plasticity development. Shear stress could also be generated at the interfaces during cement shrinkage, which was not considered in the simulation. The cement permeability could be increased if fracturing occurs in the cement during shrinkage. In this case, fracturing due to cement shrinkage would predominantly form radially from the interface with the casing (Bois et al. 2012).

5 Conclusions

In this study, the coupled hydro-mechanical finite element analysis was carried out to simulate the migration and absorption of water and bulk shrinkage behaviour of early-age cement in wellbore annulus. The main objectives are (i) to assess the threshold value of formation permeability, below which the water supply to the hardening cement becomes important, and (ii) to estimate the bulk shrinkage volume of the cement in wellbore annulus for such cases. The water absorption characteristics of the cement were calibrated based on the laboratory shrinkage test data on three different cement types found in the literature: Class G cement, rapid setting (RS) cement, and OPSD cement. The calibrated cement shrinkage parameters were incorporated into the wellbore cement shrinkage simulation where the interaction between the hardening cement and the formation was simulated. The simulation of the wellbore cement shrinkage yielded the following findings.

1. The threshold permeability of formation for providing sufficient water to hardening early-age cement is found to be 0.1 mD for the Nankai Trough case scenario. Since the formation permeability near the reservoir layer at this site could be as low as 0.01 mD, the formation would not be capable of providing sufficient water to the cement in low permeability layers.
2. The bulk shrinkage volume of OPSD cement at the Nankai Trough case would be in a range of 0.01% to 0.71%, which is related to the formation permeability between 1 mD and 0.01 mD. If Class G or RS cement were used, the bulk shrinkage volume would range from 0.02% to 1.2% (Class G cement) and from 0.01% to 1.5% (RS cement) in the same formation permeability range.
3. Whether the cement is consolidated or underconsolidated at the onset of cement initial set has a significant impact on the bulk shrinkage volume behaviour of cements. In the underconsolidated cement case, the outflux of cement pore water into the formation occurs in the initial stage which increases the bulk shrinkage volume.

This study identified a reasonable range of cement bulk shrinkage volume expected at the Nankai

Trough. This is because the shrinkage test data of OPSD cement for the Nankai Trough site was available in this study. The cases of Class G and RS cements are developed for comparison. To extend the applicability of the proposed methodology to estimate the water migration/absorption and bulk shrinkage behaviour of early-age cement in different formations, a cement shrinkage test should be conducted under tailored pressure and temperature conditions to calibrate the model parameters for expected downhole conditions.

Acknowledgements

The authors are grateful for the support provided by the MH21 Research Consortium, which facilitated the present research. We are also appreciative of the generosity of JOGMEC to provide the shrinkage test data of OPSD cement. We also thank Kaibin Qui at Schlumberger and Koji Yamamoto at JOGMEC for valuable discussion on the present work.

References

Appleby, S. & Wilson, A., 1996. Permeability and suction in setting cement. *Chemical Engineering Science*, 51(2), pp.251–267. https://doi.org/10.1016/0009-2509(95)00260-x.

Backe, K.R. et al., 1999. Characterizing Curing-Cement Slurries by Permeability, Tensile Strength, and Shrinkage. *SPE Drilling & Completion*, 14(3), pp.162–167. https://doi.org/10.2118/57712-PA.

Backe, K.R. et al., 1998. Shrinkage of Oil Well Cement Slurries. *The Journal of Cannadian Petroleum Technology*, 37(9), pp.63–67. https://doi.org/10.2118/98-09-06.

Biot, M.A., 1962. Mechanics of deformation and acoustic propagation in porous media. *Journal of Applied Physics*, 33(4), pp.1482–1498. https://doi.rog/10.1063.1.1728759.

Biot, M.A. & Willis, D.G., 1957. The elastic coefficients of the theory of consolidation. *J. Appl. Mech*, pp.594–601. https://doi.org/10.2118/139668-PA.

Bois, A. et al., 2012. Use of a Mechanistic Model To Forecast Cement-Sheath Integrity. *SPE Drilling & Completion*, 27(2), pp.303–314. https://doi.org/10.2118/139668-PA.

Bois, A.-P. et al., 2011. How to prevent loss of zonal isolation through a comprehensive analysis of microannulus formation. *SPE Drilling & Completion*, 26(1), pp.4–7. https://doi.org/10.2118/124719-PA.

Chenevert, M.E. & Shrestha, B.K., 1991. Chemical Shrinkage Properties of Oilfield Cements. *SPE Drilling Engineering*, 6(1), pp.37–43. https://doi.org/16654-PA.

Chenevert, M.E. & Shrestha, B.K., 1987. Shrinkage Properties of Cement. In *Proceedings of the 62nd Annual Technical Conference and Exhibition of the Society of Petroleum Engineers*. Dallas, Texas, pp. 49–57. https://doi.org/10.2118/16654-MS.

Coussy, O. et al., 2004. The equivalent pore pressure and the swelling and shrinkage of cement-

based materials. *Materials and Structures*, 37(265), pp.15–20. https://doi.org/10.1007/bf02481623.

Cruz, C.R. & Gillen, M., 1980. Thermal Expansion of Portland Cement Paste, Mortar and Concrete at High Temperatures. *Fire and Materials*, 4(2), pp.66–70. https://doi.org/10.1002/fam.810040203.

Fujii, T. et al., 2015. Geological setting and characterization of a methane hydrate reservoir distributed at the first offshore production test site on the Daini-Atsumi Knoll in the eastern Nankai Trough, Japan. *Marine and Petroleum Geology*, 66, pp.310–322. https://doi.org/10.1016/j.marpetgeo.2015.02.037.

Garg, S.K. & Nur, A., 1973. Effective Stress Laws for Fluid-Saturated Porous Rocks. *Journal of Geophysical Research*, 78(26), pp.5911–5921. https://doi.org/10.1029/jb078i026p05911.

Goboncan, V.C. & Dillenbeck, R.L., 2003. Real-Time Cement Expansion / Shrinkage Testing Under Downhole Conditions For Enhanced Annular Isolation. In *Proceedings of the SPE/IADC Drilling Conference*. Amsterdam, The Netherlands, pp. 1–9. https://doi.org/10.2118/79911-ms.

Gray, K.E. et al., 2007. Finite Element Studies of Near-Wellbore Region During Cementing Operations : Part I. In *Proceedings of the SPE Production and Operations Symposium*. Oklahoma City, Oklahoma, pp. 1–15. https://doi.org/10.2118/106998-MS.

Hua, C., Acker, P. & Ehrlacher, A., 1995. Analyses and models of the autogenous shrinkage of hardening cement paste. I. Modelling at macroscopic scale. *Cement and Concrete Research*, 25(7), pp.1457–1468. https://doi.org/10.1016/0008-8846(95)00140-8.

Justnes, H. et al., 1995. Chemical shrinkage of oil well cement slurries. *Advance in Cement Research*, 7(26), pp.85–90. https://doi.org/10.1680/adcr.1995.7.26.85.

Konno, Y. et al., 2015. Permeability of sediment cores from methane hydrate deposit in the Eastern Nankai Trough. *Marine and Petroleum Geology*, 66, pp.487–495. https://doi.org/10.1016/J.marpetgeo.2015.02.020.

Loiseau, A., 2014. Thermal Expansion of Cement and Well Integrity of Heavy Oil Wells. In *SPE Heavy and Extra Heavy Oil Conference*. Latin America, Medillin, Columbia, pp. 1–13. https://doi.org/10.2118/171066-MS.

Lura, P., Jensen, O.M. & Van Breugel, K., 2003. Autogenous shrinkage in high-performance cement paste: An evaluation of basic mechanisms. *Cement and Concrete Research*, 33(2), pp.223–232. https://doi.org/10.1016/s0008-8846(02)00890-6.

Lyomov, S.K. et al., 1997. Shrinkage of oil well cement slurries. *Advances in Cement Research*, 7(26), pp.85–90. https://doi.org/10.2118/97-77.

Maharidge, R. et al., 2016. Development of Permeability and Mechanical Properties of Class G Cement from Slurry to Set. In *SPE Annual Technical Conference and Exhibition, 26-28*

September, Dubai, UAE. Dubai, UAE, pp. 26–28. https://doi.org/10.2118/181512-MS.

Nishio, S., Ogisako, E. & Denda, A., 2011. Geotechnical Properties of Seabed Ground in East Nankai Trough. In *Proceedings of the 7th International Conference on Gas Hydrates (ICGH 2011)*. Edinburgh, Scotland, United Kingdom. https://doi.org/10.5026/jgeography.118.955.

Nur, A. & Byerlee, J.D., 1971. An exact effective stress law for elastic deformation of rock with fluids. *Journal of Geophysical Research*, 76(26), pp.6414–6419. https://doi.org/10.1029/jb076i026p06414

Oyarhossein, M. & Dusseault, M.B., 2015. Wellbore Stress Changes and Microannulus Development Because of Cement Shrinkage. In *Proceedings of the 49th US Rock Mechanics / Geomechanics Symposium*. San Francisco, CA, USA. ARMA-2015-118.

Parcevaux, P.A. & Sault, P.H., 1984. Cement Shrinkage and Elasticity: A New Approach for a Good Zonal Isolation. In *Proceedings of SPE Annual Technical Conference and Exhibition, held in Houston*. p. 12. https://doi.org/10.2118/13176-MS.

Qiu, K. et al., 2015. Well Integrity Evaluation for Methane Hydrate Production in the Deepwater Nankai Trough. *SPE Drilling & Completion*, 30(1), pp.52–67. https://doi.org/10.2118/174081-PA.

Ravi, K., Bosma, M. & Gastebled, O., 2002. Improve the Economics of Oil and Gas Wells by Reducing the Risk of Cement Failure. In *Proceedings of IADC/SPE Drilling Conference*. Dallas, Texas, pp. 1–13. https://doi.org/10.2118/74497-MS.

Reddy, B. et al., 2009. Cement-Shrinkage Measurement in Oilwell Cementing--A Comparative Study of Laboratory Methods and Procedures. *SPE Drilling & Completion*, 24(1), pp.104–114. https://doi.org/10.2118/103610-PA.

Rougelot, T., Skoczylas, F. & Burlion, N., 2009. Water desorption and shrinkage in mortars and cement pastes: Experimental study and poromechanical model. *Cement and Concrete Research*, 39(1), pp.36–44. https://doi.org/10.1016/j.cemconres.2008.10.005.

Saint-Marc, J., Garnier, A. & Bois, A.-P., 2008. Initial State of Stress: The Key to Achieving Long-Term Cement-Sheath Integrity. In *Proceedings of SPE Annual Technical Conference and Exhibition*. Denver, Colorado, USA. https://doi.org/10.2118/116651-MS.

Sellevold, E.J. & Bjøntegaard, Ø., 2006. Coefficient of thermal expansion of cement paste and concrete: Mechanisms of moisture interaction. *Materials and Structures*, 39, pp.809–815. https://doi.org/10.1617/s11527-006-9086-z.

Suzuki, K., Takayama, T. & Fujii, T., 2015. Density structure report from logging-while-drilling data and core data at the first offshore gas production test site on Daini-Atsumi Knoll around eastern Nankai Trough. *Marine and Petroleum Geology*, 66, pp.388–395. https://doi.org/10.1016/j.marpetgeo.2015.02.026.

Taoutaou, S. et al., 2014. Implementation of a Fit-for-Purpose Cementing Technology for the First Gas Hydrate Production in Japan. In *the International Petroleum Technology Conference*. Kuala Lumpur, Malaysia, pp. 1–15. https://doi.org/10.2523/iptc-17991-ms

Teodoriu, C. et al., 2012. Experimental Measurements of Mechanical Parameters of Class G Cement. In *Proceedings of the SPE/EAGE European Unconventional Resources Conference and Exhibition*. Vienna, Austria, pp. 20–22. https://doi.org/10.2118/153007-MS.

Thiercelin, M., Baumgarte, C. & Guillot, D., 1998. A Soil Mechanics Approach To Predict Cement Sheath Behavior. In *Proceedings of the SPE/ISRM Eurock '98*. Trondheim, Norway, pp. 329–337. https://doi.org/10.2118/14375-MS.

Thomas, J., Miller, J. & Musso, S., 2015. *Shrinkage Behavior during Early Hydration and Setting of DeepCRETE Lightweight Cement for Methane Hydrate Wells*,

Uchida, S., 2012. *Numerical investigation of geomechanical behaviour of hydrate-bearing sediments*. Ph.D. thesis, University of Cambridge.

Ulm, F.J., Constantinides, G. & Heukamp, F.H., 2004. Is concrete a poromechanics materials?-A multiscale investigation of poroelastic properties. *Materials and Structures*, 37(1), pp.43–58. https://doi.org/10.1007.bf02481626.

Vu, M.H. et al., 2012. Time-dependent behaviour of hardened cement paste under isotropic loading. *Cement and Concrete Research*, 42(6), pp.789–797. https://doi.org/10.1016/j.cemconres.2012.03.002.

Yamamoto, K. et al., 2014. Operational overview of the first offshore production test of methane hy- drates in the Eastern Nankai Trough. In *Proceedings of theOffshore Technology Conference*. Houston, Texas. https://doi.org/10.4043/25243-MS.

Yamamoto, K. et al., 2017. Thermal responses of a gas hydrate-bearing sediment to a depressurization operation. *RSC Adv.*, 7, pp.5554–5577. https://doi.org/10.4043/25243-MS.

Zhen, L. & Xiong, Y., 2013. Multiscale Chemico-Thermo-Hydro-Mechanical Modeling of Early-Stage Hydration and Shrinkage of Cement Compounds. *Journal of Materials in Civil Engineering*, 25(9), pp.1239–1247. https://doi.org/10.1061/(asce)mt.1943-5533.0000754.

Zhou, M.C., 2015. *Geomechanical study of hydrate-bearing sediments with turbidite formation and hydrate heterogeneity*. Ph.D. thesis, University of Cambridge.